Nonlinear travelling internal waves with piecewise-linear shear profiles

K. L. Oliveras^{1,†} and C. W. Curtis²

¹Mathematics Department, Seattle University, Seattle, WA 98122, USA
²Department of Mathematics and Statistics, San Diego State University, San Diego, CA 92182, USA

(Received 29 August 2017; revised 2 July 2018; accepted 30 July 2018)

In this work, we study the nonlinear travelling waves in density stratified fluids with piecewise-linear shear currents. Beginning with the formulation of the water-wave problem due to Ablowitz *et al.* (*J. Fluid Mech.*, vol. 562, 2006, pp. 313–343), we extend the work of Ashton & Fokas (*J. Fluid Mech.*, vol. 689, 2011, pp. 129–148) and Haut & Ablowitz (*J. Fluid Mech.*, vol. 631, 2009, pp. 375–396) to examine the interface between two fluids of differing densities and varying linear shear. We derive a systems of equations depending only on variables at the interface, and numerically solve for periodic travelling wave solutions using numerical continuation. Here, we consider only branches which bifurcate from solutions where there is no slip in the tangential velocity at the interface for the trivial flow. The spectral stability of these solutions is then determined using a numerical Fourier–Floquet technique. We find that the strength of the linear shear in each fluid impacts the stability of the corresponding travelling wave solutions. Specifically, opposing shears may amplify or suppress instabilities.

Key words: instability, internal waves, stratified flows

1. Introduction

As noted in Appel (2004) and Helfrich & Melville (2006), internal waves are known to be a common feature in coastal oceanic flows. Resulting from instabilities along pynoclines and thermoclines, internal waves with amplitudes from 5–100 m have been observed (Osborne & Burch 1980; Appel 2004; Helfrich & Melville 2006). While several generation mechanisms have been proposed and studied, it appears that in most cases internal waves are generated in coastal regions due to the presence of tide induced shearing forces in stratified fluids moving over varying bathymetry (Farmer & Armi 1999; Helfrich & Melville 2006). What is interesting though is that, while depth varying shear currents should be anticipated in such environments, most modelling attempts have traditionally ignored the impact of vorticity on internal wave dynamics. This work will address this shortcoming in part by studying the impact of depth varying shear currents on the existence and flow properties of internal travelling wave solutions (TWSs) in density stratified environments.

While the impact of vorticity on internal waves is not well understood, a great deal of work on the influence of shear in free-surface flows has appeared. The simplest case of free surfaces moving over depth varying currents is when the vorticity is assumed to be a constant throughout the fluid. The literature on this subject is too vast to address here, although we point out the seminal studies of Simmen & Saffman (1985), da Silva & Peregrine (1988), Vanden-Broeck (1994) and the extensive bibliography in Constantin (2011). We also note that a key part of the approach we take in this paper follows the work in Ashton & Fokas (2011), which in part makes use of the unified transform method (UTM) pioneered in Fokas (2008).

Perhaps surprisingly, there are still outstanding and significant issues even for constant vorticity flows. In particular, the impact of vorticity on the stability of travelling wave solutions is not fully understood. As shown in Oliveras, Sprenger & Vasan (2016), vorticity modifies the amplitudes of Benjamin-Feir (BF) instabilities depending on the sign of the vorticity. Similar results have analytically been found in approximate models (Choi 2009; Thomas, Kharif & Manna 2012; Hur & Johnson 2015). In addition, constant vorticity introduces 'high-frequency' instabilities similar to those observed in irrotational waves (see McLean 1982b; Francius & Kharif 2006; Deconinck & Oliveras 2011). These instabilities may be more dominant than the BF instability depending on the amplitude of the TWS and the strength of the linear shear as shown in Oliveras et al. (2016). Furthermore, for a TWS with a region of lower pressure trapped under the wave (da Silva & Peregrine 1988; Vasan & Oliveras 2014), new instabilities, perhaps related to a Rayleigh-Taylor instability, are visible in the spectrum. As shown in Vasan & Oliveras (2014), the existence of these low pressure regions is directly related to the existence of stagnation points within the fluid. While usually avoided in much of the existing literature due to the analytic difficulties they introduce, it is becoming clearer that stagnation points can have significant impacts on wave shape and stability. Thus, in part due to stagnation point induced low pressure regions, and in part due to high-frequency instabilities, no TWSs have been found which are stable to all perturbations despite the ability of a constant shear current to suppress the onset of BF instabilities.

Given these results for constant vorticity, it is interesting then to ask how depth variation in the vorticity affects the existence of these instabilities, and whether more complicated shear profiles will support the existence of stable internal or even free-surface travelling waves. The case of non-constant vorticity flows has received far less attention. For the case of non-steady waves, this was first examined in Dalrymple (1974) for a stratified fluid with two differing densities ρ_1 and ρ_2 and two differing constant vortices ω_1 and ω_2 . We refer to such fluids as bistratified; see figure 1 for reference. More recently, such systems have been looked at experimentally and numerically (Swan, Cummins & James 2001; Ko & Strauss 2008). Assuming a rigid lid and zero vorticity, i.e. $\omega_2 = 0$, in the lower fluid region, nonlinear, large amplitude travelling interfacial waves for bistratified fluids were studied (see Pullin & Grimshaw 1983, 1988). A complete characterization of the linear stability of the small amplitude limit of these waves was presented in Pullin & Grimshaw (1986). Generalizing this work, the evolution of a free surface and a free internal layer for a bistratified fluid in a shallow-water approximation was studied in Curtis, Oliveras & Morrison (2016). Significant nonlinear phenomena like internal dispersive shock waves as a result of bistratification was reported for the first time.

Focusing then on the case of single-valued internal layers, by assuming a rigid lid at the fluid-air interface and an impermeable sea bed, using the UTM techniques (Haut & Ablowitz 2009; Ashton & Fokas 2011) and incorporating techniques developed

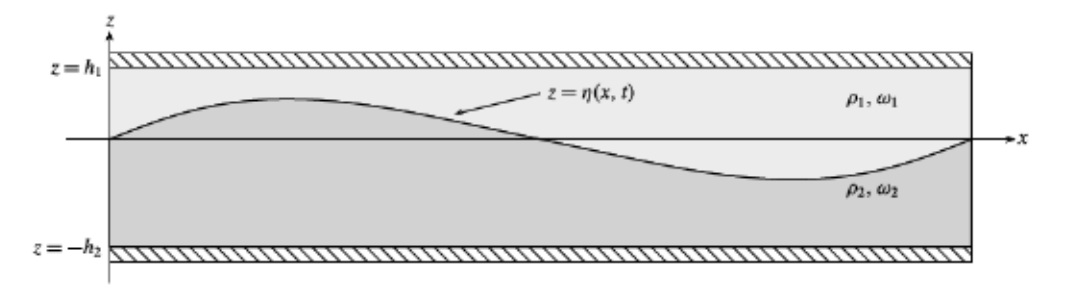


FIGURE 1. Fluid domain for the rigid lid problem.

for travelling wave solutions (Oliveras & Vasan 2013), we derive a closed system describing the evolution of the free internal surface in a bistratified fluid. Using this formulation, we can analytically determine at which wave speeds bifurcations from flat states will occur. By developing a Stokes expansion at this bifurcation point, we can analytically determine the behaviour of the bifurcation curve in terms of wave height and speed in a small-amplitude limit, thereby allowing for a better understanding of when stagnation points in the fluid velocity appear and when turning points in bifurcation curves appear.

We then use numerical continuation to generate bifurcation curves which provide the speed-amplitude relationship for the travelling nonlinear interfacial waves. Of particular interest is the role different choices of vorticities play in determining the number of stagnation points within the fluid regions, and how these stagnation points influence the shape and properties of the interfacial TWSs. As we show, the position and number of stagnation points determines whether waves are elevated, depressed, symmetric in nature or especially peaked. To complement these results, we also present plots of the streamlines to help illustrate the different impacts on the dynamics that the stagnation points have throughout the bulk of the fluid as well as on the interface.

Finally, we study the stability of various TWSs. One of the most striking features associated with bistratification is the complicated relationship between the appearance of modulational instabilities (MIs) and the choices of the shear strength and depth ratio of the layers. As we show, by making the ratio of the depths of the two layers large enough, MIs appear to be completely suppressed. However, we also show results in which MIs are introduced and suppressed by shear, thereby illustrating the complicated balances mediated by nonlinearity between these parameter choices. These results generalize and expand on those for constant vorticity in single-layer fluids, in which vorticity is shown to strongly influence whether MIs exist (Pullin & Grimshaw 1986; Thomas *et al.* 2012; Oliveras *et al.* 2016).

However, at least for the solutions examined in this paper, all travelling solutions are unstable with respect to higher-frequency perturbations corresponding to resonant interactions (or *n*-wave mixing). Given the more complicated nature of the physical problem studied in this paper, it is a non-trivial question to determine if all travelling wave solutions are unstable, especially given the stabilizing mechanisms we illustrate via our numerical result. Likewise, the complex nature of instabilities for multi-valued interfaces remain unknown and will be explored in future work.

The structure of the paper is as follows. The derivation of our model is given in § 2. The computation of the TWSs and analytic derivations of the nonlinear impact on wave speed and the presence of stagnation points are given in § 3. Section 4 explains

the means by which we numerically determine the stability of the TWSs computed in this paper, and § 5 contains the results of these stability computations. Concluding remarks appear in § 6, and the appendices collect the technical details used throughout the paper.

2. Boundary conditions and AFM formulation

We assume the flow is incompressible in each region in a frame of reference moving to the right with speed c. The resulting equations must satisfy Euler's equations in the bulk:

$$\nabla \cdot u_j = 0, \tag{2.1}$$

$$\partial_t u_j + (u_j \cdot \nabla) u_j = -\frac{1}{\rho_j} \nabla p_j - g\hat{z},$$
 (2.2)

where $u_j = (u_j - c, w_j)^T$ and j = 1, 2 correspond to the fluid velocities in the top and bottom layer of the fluid respectively, $p_j = p_j(x, z)$ is the pressure at any point within each fluid, ρ_j is the density of each fluid and g is the constant acceleration due to gravity.

At the interface between each fluid, we require continuity in pressure, as well as continuity in the normal velocities of each fluid at the interface. This provides the boundary conditions

$$p_1 = p_2$$
 and $u_1 \cdot N = u_2 \cdot N$ at $z = \eta(x, t)$, (2.3a,b)

where N represents a unit normal vector to the interface defined by $z = \eta(x, t)$. Furthermore, the interface is evolved by the fluid velocities normal to the interface. That is,

$$\eta_t = u_i \cdot N, \tag{2.4}$$

for j = 1 or j = 2 as they are equivalent. Finally, the rigid lid and solid boundary conditions require

$$v_1 = 0$$
 at $z = h_1$, $v_2 = 0$ at $z = -h_2$. (2.5a,b)

2.1. A non-local formulation

Equations (2.1)–(2.5) represent the equations we wish to solve provided that there is a constant linear shear within each fluid domain. That is, that

$$\partial_x w_i - \partial_z u_i = \omega_i$$
 (2.6)

within each fluid where we have chosen a particular sign convention for the vorticity consistent with conventions used elsewhere in the literature (see da Silva & Peregrine 1988; Ko & Strauss 2008). A disadvantage of the above formulation is that it requires one to solve for the velocities and pressure within the bulk of each fluid as well as the interface separating the two fluids. In our work, we choose to cast the equations of motion using a non-local reformulation that allows us to work completely within the context of variable defined at the interface. Here we follow the work of Haut & Ablowitz (2009), Ashton & Fokas (2011) in order to recast the problem into variables defined at the interface. However, to take advantage of this formulation, we first pose (2.1)–(2.5) in terms of new bulk variables.

Let ψ_j for j = 1, 2 represent the streamfunctions in the top and bottom layer of the fluid respectively. Furthermore, we introduce the functions ϕ_j for j = 1, 2 to represent the contributions to the velocity from potential flow. Thus, we can write the fluid velocities as

$$\begin{pmatrix} u_j - c \\ w_j \end{pmatrix} = \begin{pmatrix} \partial_x \phi_j - \omega_j z \\ \partial_z \phi_j \end{pmatrix} = \begin{pmatrix} \partial_z \psi_j \\ -\partial_x \psi_j \end{pmatrix}. \tag{2.7}$$

Using (2.1)-(2.5), the streamfunctions and potential functions satisfy

$$\Delta \phi_i = 0$$
, $(x, z) \in D_i$, (2.8)

$$\Delta \psi_i = -\omega_i \quad (x, z) \in D_i,$$
 (2.9)

$$\partial_t \phi_j + \omega_j \psi_j + \frac{1}{2} |\nabla \phi_j - \omega_j z \hat{\mathbf{x}}|^2 + \frac{p_j}{\rho_j} + gz = 0, \quad (x, z) \in D_j$$
 (2.10)

within the bulk of each fluid.

Remark 1. In integrating (2.2) within the fluid domain to find (2.10), we arrive at an equation of the form

$$\partial_t \phi_j + \omega_j \psi_j + \frac{1}{2} |\nabla \phi - \omega_j z \hat{\mathbf{x}}|^2 + \frac{p_j}{\rho_j} + gz = B_j(t), \tag{2.11}$$

where we call the time varying function $B_j(t)$ the Bernoulli function. However, by introducing the change of variables

$$\phi_j = \tilde{\phi}_j + \int_0^t B_j(s) \, \mathrm{d}s, \qquad (2.12)$$

we can eliminate the Bernoulli function, and thus we set it to zero throughout the remainder of this text.

2.2. Non-local formulation in interface quantities

Following the work of Ablowitz, Fokas & Musslimani (2006), Haut & Ablowitz (2009), Ashton & Fokas (2011), we introduce the harmonic functions φ_j such that

$$\varphi_i = e^{-ikx} \cosh(k(z + (-1)^j h_i)).$$
 (2.13)

Noting that

$$(\partial_z \varphi_j)(\Delta \psi_j + \omega_j) + \partial_z \psi_j(\Delta \varphi_j) = 0,$$
 (2.14)

where ψ_j solves (2.9), we integrate the above quantity over the respective fluid domain. By using Green's second identity and integration by parts, we can readily show that for j = 1, 2.

$$\int_{0}^{2\pi L} e^{-ikx} ((ik(\partial_{t}\eta) - \omega_{j})C_{j} - k(\partial_{x}q_{j} - \omega_{j}\eta)S_{j}) dx = 0, \quad \forall k \in \Lambda,$$
(2.15)

where $\Lambda = \{k = (2n\pi)/L | n \in \mathbb{Z}/\{0\}\}, q_j \text{ is given by }$

$$q_i(x, t) = \phi_i(x, \eta(x, t), t),$$
 (2.16)

and the quantities C_i , S_i are defined by

$$C_j = \cosh(k(\eta + (-1)^j h_j)), \quad S_j = \sinh(k(\eta + (-1)^j h_j)).$$
 (2.17*a,b*)

Using the boundary condition

$$p_1(x, \eta, t) = p_2(x, \eta, t),$$
 (2.18)

along with our new variables q_i we also find j = 1, 2, we have

$$\partial_{t}q_{1} - \omega_{1}\partial_{x}^{-1}\partial_{t}\eta + \frac{1}{2}(\partial_{x}q_{1} - \omega_{1}\eta)^{2} - \frac{1}{2}\frac{(\partial_{t}\eta + \partial_{x}\eta(\partial_{x}q_{1} - \omega_{1}\eta))^{2}}{1 + (\partial_{x}\eta)^{2}} + g\eta
= \rho\left(\partial_{t}q_{2} - \omega_{2}\partial_{x}^{-1}\partial_{t}\eta + \frac{1}{2}(\partial_{x}q_{2} - \omega_{2}\eta)^{2} - \frac{1}{2}\frac{(\partial_{t}\eta + \partial_{x}\eta(\partial_{x}q_{2} - \omega_{2}\eta))^{2}}{1 + (\partial_{x}\eta)^{2}} + g\eta\right).$$
(2.19)

Thus, (2.15) for j = 1, 2 along with (2.19) represent a closed system of three equations for the three unknown quantities (q_1, q_2, η) .

2.3. Non-dimensionalization

Introducing the non-dimensional parameters given by

$$\tilde{x} = \frac{x}{L}$$
, $\tilde{z} = \frac{z}{h_1}$, $\tilde{t} = \frac{c_0}{L}t$, $q_j = \epsilon c_0 L \tilde{q}_j$, $\eta = a\tilde{\eta}$, $\tilde{k} = Lk$, (2.20a-f)

and

$$\tilde{\omega}_j = \omega_j \frac{h_1}{c_0}, \quad \tilde{c} = \frac{c}{c_h}, \quad \mu = \frac{h_1}{L}, \quad \epsilon = \frac{a}{h_1}, \quad \delta = \frac{h_2}{h_1},$$
 (2.21a-e)

where $c_h = \sqrt{gh_1}$, we have the following system of three equations

$$\partial_{t}(q_{1} - \omega_{1}\partial_{x}^{-1}\eta) + \frac{\epsilon}{2}(\partial_{x}q_{1} - \omega_{1}\eta)^{2} + \eta - \frac{\epsilon\mu^{2}}{2}\frac{(\partial_{t}\eta + (\epsilon\partial_{x}\eta)(\partial_{x}q_{1} - \omega_{1}\eta))^{2}}{1 + (\epsilon\mu\partial_{x}\eta)^{2}} \\
= \rho\left(\partial_{t}(q_{2} - \omega_{2}\partial_{x}^{-1}\eta) + \frac{\epsilon}{2}(\partial_{x}q_{2} - \omega_{2}\eta)^{2} + \eta - \frac{\epsilon\mu^{2}}{2}\frac{(\partial_{t}\eta + (\epsilon\partial_{x}\eta)(\partial_{x}q_{2} - \omega_{2}\eta))^{2}}{1 + (\epsilon\mu\partial_{x}\eta)^{2}}\right), \tag{2.22}$$

$$\int_{0}^{2\pi} e^{-ikx} ((ik\epsilon \mu^{2} \partial_{t} \eta - \omega_{1}) C_{1} - \epsilon \mu k (\partial_{x} q_{1} - \omega_{1} \eta) S_{1}) dx = 0, \quad \forall k \in \mathbb{Z}/\{0\}, \quad (2.23)$$

and

$$\int_{0}^{2\pi} e^{-ikx} ((ik\epsilon \mu^{2} \partial_{t} \eta - \omega_{2}) C_{2} - \epsilon \mu k (\partial_{x} q_{2} - \omega_{2} \eta) S_{2}) dx = 0, \quad \forall k \in \mathbb{Z}/\{0\}. \quad (2.24)$$

3. Travelling wave equations

Working with the non-dimensional equations in a travelling coordinate frame, letting $\partial_t \eta \to -c\partial_x \eta$ as well as $\partial_t q_j \to -\partial_x q_j$ for j=1,2, the equations for stationary solutions in a travelling frame become

$$\left(\frac{1}{2}\frac{(\epsilon(\partial_x q_1 - \omega_1 \eta) - c)^2}{1 + (\epsilon \mu \partial_x \eta)^2} + \epsilon \eta - \frac{1}{2}c^2\right) = \rho \left(\frac{1}{2}\frac{(\epsilon(\partial_x q_2 - \omega_2 \eta) - c)^2}{1 + (\epsilon \mu \partial_x \eta)^2} + \epsilon \eta - \frac{1}{2}c^2\right),$$
(3.1)

$$\int_0^{2\pi} e^{-ikx} (\mathcal{C}_1 \omega_1 + \mu k \mathcal{S}_1 (\epsilon (\partial_x q_1 - \omega_1 \eta) - c)) dx = 0, \tag{3.2}$$

$$\int_{0}^{2\pi} e^{-ikx} (C_2 \omega_2 + \mu k S_2(\epsilon (\partial_x q_2 - \omega_2 \eta) - c)) dx = 0, \qquad (3.3)$$

where $C_j = \cosh(\mu k(\epsilon \eta + d_j))$ and $S_j = \sinh(\mu k(\epsilon \eta + d_j))$ with $d_1 = -1$ and $d_2 = \delta$. In the above formulation, we are required to solve three equations for three unknown functions η , q_1 and q_2 . However, as in Ashton & Fokas (2011), Deconinck & Oliveras (2011), we can reduce the dimensionality of the problem by formally solving the Bernoulli equation for either the quantity $\epsilon \partial_x q_1 - \epsilon \omega_1 \eta - c$ or $\epsilon \partial_x q_2 - \epsilon \omega_2 \eta - c$. Without loss of generality, we solve for the tangential velocity approaching the interface from above $\partial_x q_1$ in terms of $\partial_x q_2$ to find

$$\epsilon(\partial_x q_1 - \omega_1 \eta) - c = \sigma \sqrt{\rho(\epsilon \partial_x q_2 - \epsilon \omega_2 \eta - c)^2 + (c^2 - 2\epsilon \eta)(1 + (\epsilon \mu \partial_x \eta)^2)(1 - \rho)},$$
(3.4)

where $\sigma = \pm 1$.

Remark 2. The meaning of the plus/minus sign is typically of critical importance in problems involving linear shear (see Vasan & Oliveras 2014). However, when simply solving for the interface variables η and q_2 , an alternative choice in σ is equivalent to changing the sign of vorticity in the upper layer given by ω_1 . Furthermore, to ensure that $(\eta, q_1, q_2) = (0, 0, 0)$ remains a solution to the problem, that is, that we consider travelling wave solutions that bifurcate from flat water with no jump in the tangential velocity, we choose $\sigma = -\text{sgn}(c_0)$ as indicated by (3.4) where c_0 is the speed corresponding to bifurcation from the trivial solution.

The resulting equations to solve for $\eta(x)$ and $q_2(x)$ are given by

$$\int_{0}^{2\pi} e^{-ikx} \left(C_{1}\omega_{1} + \mu k S_{1} \right)$$

$$\left(\sigma \sqrt{\rho(\epsilon \partial_{x}q_{2} - \epsilon \omega_{2}\eta - c)^{2} + (c^{2} - 2\epsilon \eta)(1 + (\epsilon \mu \partial_{x}\eta)^{2})(1 - \rho)} \right) dx = 0, \quad (3.5)$$

$$\int_{0}^{2\pi} e^{-ikx} (C_{2}\omega_{2} + \mu k S_{2}(\epsilon(\partial_{x}q_{2} - \omega_{2}\eta) - c)) dx = 0, \quad (3.6)$$

where C_j and S_j are the same as given before this system of two equations can be solved for the unknowns η and $\partial_x q_2$ for an admissible value of the wave speed c. Once solutions for η and $\partial_x q_2$ are determined, $\partial_x q_1$ is obtained directly by substitution in (3.4).

3.1. Bifurcation from trivial flow

Since we ultimately use a numerical continuation scheme in this work, we determine for which wave speeds c a non-trivial solution will bifurcate from the zero solution. This is achieved by expanding the free surface η , $\partial_x q_2$ and c in powers of ϵ of the form

$$\eta(x) = \sum_{n=0}^{\infty} \epsilon^n \eta_n(x), \quad \partial_x q_2 = \sum_{n=0}^{\infty} \epsilon^n \partial_x v_n, \quad c = \sum_{n=0}^{\infty} \epsilon^n c_n.$$
 (3.7*a*-*c*)

We assume that solutions will bifurcation from a wave with positive velocity so that $c_0 > 0$ and thus, choosing $\sigma = -1$ enforces bifurcating from a branch where there is no jump in the tangential velocity. Similarly, we consider a frame of reference such that $q_2(x)$ has zero-average value. Expanding (3.5) and (3.6) in ϵ , we find the following linear system for η_0 and v_0 given by

$$\begin{pmatrix}
\mu k c_0^2 - \tanh(\mu k)(\tilde{\omega}c_0 - (\rho - 1)) & c_0 \rho \tanh(\mu k) \\
-\mu k c_0 & \tanh(\delta \mu k)
\end{pmatrix}
\begin{pmatrix}
\mathcal{F}_k \{\eta_0\} \\
\mathcal{F}_k \{v_0\}
\end{pmatrix}$$

$$= c_1 \begin{pmatrix}
\mathcal{F}_k \{c_0 \tanh(\mu k)\} \\
-\mathcal{F}_k \{\tanh(\delta \mu k)\}
\end{pmatrix}, \tag{3.8}$$

where $\mathcal{F}_k\{f(x)\}$ represents the kth Fourier coefficient of f(x) defined by

$$\mathcal{F}_{k} \{f(x)\} = \frac{1}{2\pi} \int_{0}^{2\pi} e^{-ikx} f(x) dx, \qquad (3.9)$$

and we have introduced the quantity $\tilde{\omega} = \omega_1 - \rho \omega_2$.

Since the right-hand side of (3.8) evaluates to zero, we can then say that the only way for there to be a non-zero solution for η_0 and v_0 is for the linear operator on the left-hand side of (3.8) singular for at least one k value (henceforth referred to as k_0). This leads to the equation c_0 given by

$$c_0^2 - \tilde{\omega} T_{k_0} c_0 - T_{k_0} (\rho - 1) = 0,$$
 (3.10)

where

$$T_k = \frac{\tanh(\mu k) \tanh(\delta \mu k)}{\mu(\rho \tanh(\mu k) + \tanh(\delta \mu k))}.$$
(3.11)

Using this notation, we find

$$c_0 = \frac{\Omega(k_0)}{k_0}, \quad \Omega(k_0) = \frac{1}{2} \left(-\mathcal{T}_{k_0} \tilde{\omega} + \operatorname{sgn}(k_0) \sqrt{\mathcal{T}_{k_0}^2 \tilde{\omega}^2 + 4(\rho - 1)k_0 \mathcal{T}_{k_0}} \right), \quad (3.12a, b)$$

where the negative solution is extraneous due to our earlier assumptions of bifurcating from a positive speed c_0 .

The corresponding non-trivial solutions are given by

$$\eta_0(x) = \cos(k_0 x), \quad v_0(x) = \frac{\mu k_0 c_0}{\tanh(\mu \delta k_0)} \cos(k_0 x).$$
 (3.13*a*,*b*)

Thus, for a given wave-number k_0 , the leading-order approximations to the solution set $(\eta(x), \partial_x q_2, c)$ are given by the expressions in (3.12a,b) and (3.13a,b). With the

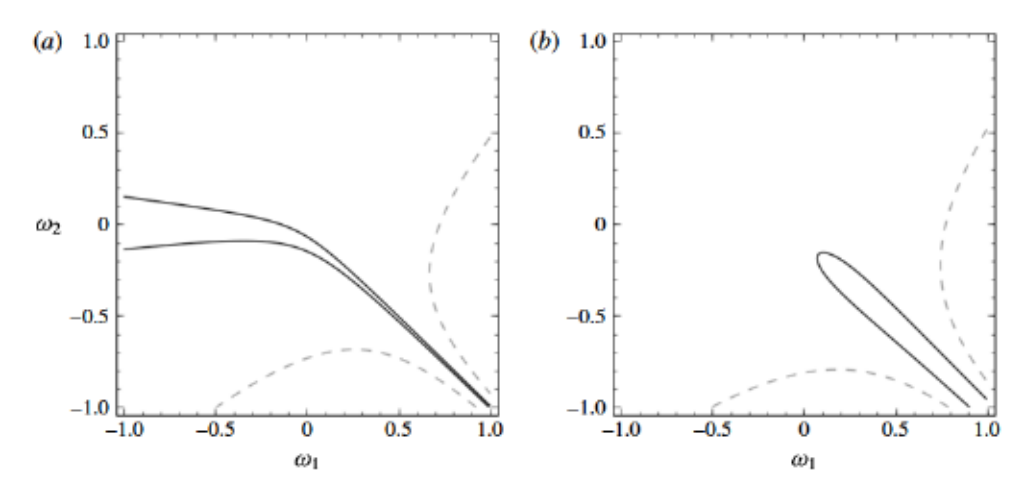


FIGURE 2. Plots of c_2 for $\rho=1.028$, $\mu=\sqrt{0.1}$, $\delta=4$ and $k_0=1$ (a) and $k_0=10$ (b). In (a,b) the solid (-) line denotes the $c_2=0$ contour, with the interior of these curves marking the regions for which $c_2<0$. In (a) the dashed curve (--) denotes the $c_2=10^6$ contour, while in (b) it denotes the $c_2=10^4$ contour.

aid of a computer algebra system, we determine higher-order corrections to the speed c whereby

$$c \approx c_0 + \epsilon^2 c_2 + O(\epsilon^4)$$
. (3.14)

By finding c_2 , we can generate analytic results which provide insight into the impact of vorticity on the speed at which the interface propagates. Specifically, we see that c_2 can change sign relative to c_0 for different vorticities. Furthermore, we will later see a strong connection between the sign of c_2 and the overall shape of the interface.

Figure 2 shows the regions where c_2 changes signs. As seen in the figure, the response of c_2 to the choice of vorticities can be quite sensitive. For example, choosing a weak stratification value of $\rho=1.028$, reflective of oceanic density stratification, $\mu=\sqrt{0.1}$, $\delta=4$ and choosing the $c_{0,+}$ branch, we plot c_2 in figure 2 for $k_0=1$ and $k_0=10$. While both plots exhibit a wide range of scales with respect to the magnitude of c_2 , this range is far wider for $k_0=1$ than $k_0=10$. Likewise, the region over which c_2 is negative is far larger in the case for $k_0=1$. Note, those regions for which $c_2<0$ are regions in which the wave speed decreases with increasing wave height, which is in contrast to the usual result whereby nonlinear wave speed increases with increasing wave height. Furthermore, we will later see a strong connection between the sign of c_2 and the overall shape of the interface.

3.2. Stagnation points

Given their connections to high pressure regions, the presence of stagnation points interior to each of the fluid domains impacts both the shape and stability of travelling wave solutions. We proceed to find conditions for the presence of stagnation points interior to each of the fluid domains. In order for there to be a stagnation point inside the fluid domain, there must exist a point inside the domain such that u-c=0. For simplicity, let $z_j^{(s)}$ represent the location of a stagnation point inside the upper (j=1) or lower (j=2) fluid domain so that $0 \le z_1^{(s)} \le 1$ and $-\delta \le z_2^{(s)} \le 0$. At leading order,

it is straightforward to show that the relative horizontal profile u-c is given by

$$u - c = -\omega_j z - c_0 + O(\epsilon) \qquad (3.15)$$

inside of each fluid domain implying that stagnation will occur if there is a z inside each fluid domain such that $-\omega_i z = c_0$.

For example, in the upper fluid domain, the condition for the existence of a stagnation point is given by

$$-\omega_1 z_1^{(s)} = c_0^{\pm} \rightarrow z_1^{(s)} = \frac{c_0^{\pm}}{-\omega_1}.$$
 (3.16)

From this perspective, it is clear that there will only be a stagnation point inside the upper fluid domain provided that $sgn(\omega_1) = -sgn(c_0^{\pm})$. Likewise, there will only be a stagnation point inside the lower fluid domain provided that $sgn(\omega_2) = sgn(c_0^{\pm})$. By enforcing the condition that the stagnation point is inside the appropriate fluid domain, we find the following conditions for the existence of a stagnation point when $c_0 = c_0^{+}$:

Upper fluid domain:
$$\omega_1 > \frac{\rho \omega_2 \mathcal{T}_{k_0} - \sqrt{\rho^2 \omega_2^2 \mathcal{T}_{k_0}^2 + 4 \mathcal{T}_{k_0} (\mathcal{T}_{k_0} + k_0) (\rho - 1)}}{2(\mathcal{T}_{k_0} + k_0)},$$
Lower fluid domain: $\omega_2 < \frac{\omega_1 \delta \mathcal{T}_{k_0} + \sqrt{\omega_1^2 \delta^2 \mathcal{T}_{k_0}^2 + 4 \delta \mathcal{T}_{k_0} (\rho \mathcal{T}_{k_0} + \delta k_0) (\rho - 1)}}{2\delta(\rho \mathcal{T}_{k_0} + \delta k_0)}.$
(3.17)

Figure 3 shows the regions in the (ω_1, ω_2) plane where stagnations points are found in the upper, lower or both fluid domains. Depending on the configuration of ω_1 and ω_2 the presence of the stagnation points for the trivial solution from which we continue greatly impact the shape of the solutions along the corresponding bifurcation branch. These various configurations will be contrasted in the next section with travelling wave solutions.

3.3. Constructing solutions: numerical implementation

Using the above formulation, we numerically determine travelling wave solutions by solving for the set $(\eta, \partial_x q_2, c)$ for solutions with a fixed spatial period L and for fixed wave height $\|\eta\|_{\infty}$. In the following section, we outline the specific details of the numerical implementation of our pseudo-arclength continuation method. (Code is available on GitHub.)

To numerically solve (3.5) and (3.6), we use a pseudospectral method to solve for the Fourier coefficients of our unknown functions η and $\partial_x q_2$ – differentiation is conducted in Fourier space, while nonlinear operations are computed in physical space. Since we are considering 2π periodic solutions, we numerically represent η and $\partial_x q_2$ by their Fourier series representation with N Fourier modes of the form

$$\eta(x) = \sum_{n=-N}^{N} \hat{\eta}_n e^{ik_n x}, \quad \partial_x q_2(x) = \sum_{n=-N}^{N} \hat{Q}_n e^{ik_n x}, \quad (3.18a,b)$$

where the ' denotes the summation with $n \neq 0$ as we have eliminated both the average value of η as well as the average value of $\partial_x q_2$. Enforcing $\partial_x q_2$ has zero average,

we consider zero-mean flow in both the upper and lower fluid. Thus, both η and $\partial_x q_2$ are represented by 2N unknown Fourier coefficients.

Evaluating equations (3.5) and (3.6) for $k = k_{-N}, \ldots, k_{-2}, k_{-1}, k_1, k_2, \ldots, k_N$ generates $2 \times (2N)$ equations for the $2 \times (2N)$ unknowns $\hat{\eta}_n$ and \hat{Q}_n for $n = -N, \ldots, -1, 1, \ldots, N$. In order to solve for travelling waves solutions with various amplitudes, we enforce a fixed amplitude for the interface η by allowing the wave speed c to vary as a function of the amplitude, thereby introducing both a new equation and new unknown into our system.

Equations (3.5)–(3.6) are solved for $(\hat{\eta}, \hat{Q}, c)$ iteratively via Newton's method (although other iterative techniques can also be used). Using a pseudo-arclength continuation, we determine travelling wave solutions for increasingly larger amplitudes.

Remark 3. Due to the exponential nature of the hyperbolic sine and cosine functions, we rewrite the quantities C_i and S_i for i = 1, 2 as follows

$$C_1 = \cosh(\mu k(\epsilon \eta - 1)) = \cosh(\mu k)(\cosh(\mu k \epsilon \eta) - \tanh(\mu k) \sinh(\mu k \epsilon \eta)), \quad (3.19)$$

$$S_1 = \sinh(\mu k(\epsilon \eta - 1)) = \cosh(\mu k)(\sinh(\mu k \epsilon \eta) - \tanh(\mu k) \cosh(\mu k \epsilon \eta)). \quad (3.20)$$

3.3.1. Visualizing streamlines and pressure contours

For periodic travelling wave solutions, the solutions for the streamlines take the form

$$\psi_j = a_0 + a_1(z + (-1)^j \delta_j) - \frac{\omega_j}{2} (z + (-1)^j \delta_j)^2 + \sum_{k = -\infty}^{\infty} e^{ikx} \hat{\psi}_k^{(j)} \sinh(k(z + (-1)^j \delta_j)). \quad (3.21)$$

Choosing the non-dimensional function

$$\varphi_j = e^{-ikx} \cosh(\mu k(z + (-1)^j \delta_j)), \tag{3.22}$$

where $\delta_1 = 1$, and $\delta_2 = \delta$, then the analogue of (2.15) for stationary solutions in a travelling frame is, for $k \neq 0$, given by

$$\int_{0}^{2\pi} e^{-ikx} \left(\cosh(\mu k (\epsilon \eta + (-1)^{j} \delta_{j})) (\partial_{x} q_{j} - \omega_{j} \eta - c) + \frac{\omega}{k} \sinh(\mu k (z + (-1)^{j} \delta_{j})) \right) dx$$

$$= \int_{0}^{2\pi} e^{-ikx} \partial_{z} \psi_{j}(x, (-1)^{j} \delta_{j}) dx$$
(3.23)

whereas for k = 0, we find

$$\int_0^{2\pi} \partial_z \psi_j(x, (-1)^j \delta_j) \, dx = \int_0^{2\pi} e^{-ikx} (\partial_x q_j - c) \, dx.$$
 (3.24)

Once we have determined a TWS corresponding to the set (η, q_1, q_2, c) , we can then use the above equations to determine the streamfunction within the bulk of each fluid by solving for the coefficient a_1 as well as $\hat{\psi}_k^{(j)}$. We also note that the streamfunction ψ can only be determined up to an arbitrary constant within the fluid domain. Here we choose to normalize so that the streamfunctions are zero on the interface. This flexibility allows us to determine the value of a_0 .

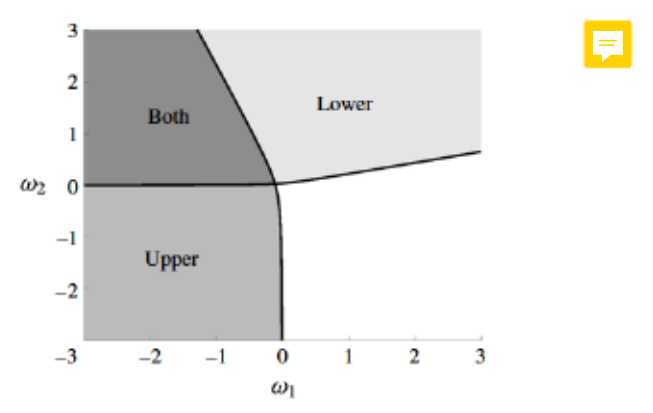


FIGURE 3. Vorticity strengths that yield a stagnation point in the upper fluid, lower fluid or in both for $\mu = \sqrt{0.1}$, $\rho = 1.028$ and $\delta = 4$.

3.4. The irrotational case

Before we investigate the effects of shear in each layer, we begin by investigating solutions with no shear (vorticity) in each layer. In figure 4, we examine the weak stratifications for $\rho=1.028,~\mu=\sqrt{0.1}$ and various values of the depth ratio δ . For $\delta=0.5$, as we increase the amplitude, both the speed of the travelling wave and the interface become more peaked. However, as δ increases from $\delta=0.5$ to $\delta=2$, both the amplitude–speed dependence and qualitative shape of the solution undergo transformation.

Specifically, for $\delta=0.5$, waves with larger amplitude travel at higher speeds. However, as δ increases, this relationship changes so that waves of larger amplitude travel at slower speeds than those with lower amplitudes. As δ continues to increase, the amplitude–speed relationship continues to change until the waves with larger amplitudes again travel at larger speeds. Simultaneously, the qualitative shape of solutions morph from 'peaked waves of elevation', through rounded peaks and troughs, and finally to 'peaked waves of depression'. This transition can be accurately predicted by examining how the sign of c_2 varies with respect to μ and δ for a specific value of ρ as seen in figure 5.

3.5. Including shear effects

We now consider the influence of linear shear within each fluid layer. In particular, we focus on the difference between the shape of solutions and the overall bifurcation structure of travelling wave solutions. Specifically, we examine solutions for $\delta=4$, $\rho=1.028$ and $\mu=\sqrt{0.1}$ that bifurcate from trivial flows that various configurations of stagnation points within each layer of the fluid.

Noting that we numerically solve for both the free surface η and the tangential velocity $q_2(x)$, we can conjecture a limiting wave height by imposing that $q_1(x)$.

3.5.1. No stagnation points in either fluid

To look at an example in which we bifurcate from a flat surface with a stagnation point in the lower fluid, we choose $\omega_1 = 1$ and $\omega_2 = -1$. As seen in figure 6(a,b), the absence of stagnation points does not appear to bias the interface towards elevation or depression, thus allowing for the development of far more symmetric nonlinear wave profiles than are seen in subsequent sections. We also note that, by referring

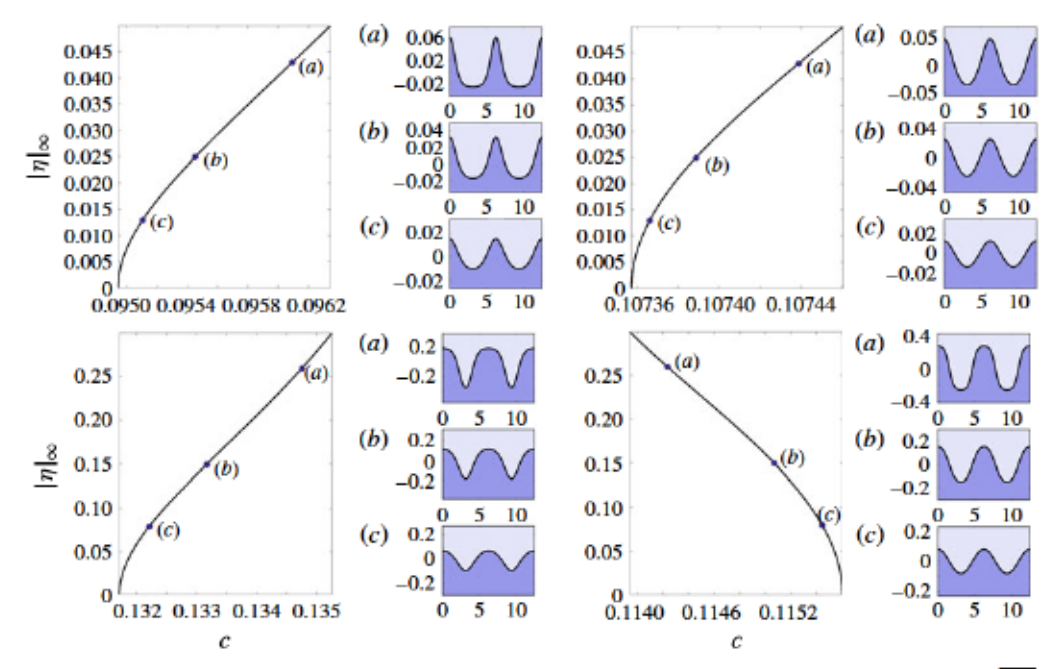


FIGURE 4. (Colour online) Bifurcation curves and solutions for $\omega_1 = \omega_2 = 0$, $\mu = \sqrt{0.1}$ and $\rho = 1.028$ and $\delta = 0.5$, $\delta = 0.75$, $\delta = 1$ and $\delta = 2$ starting clockwise from the top.

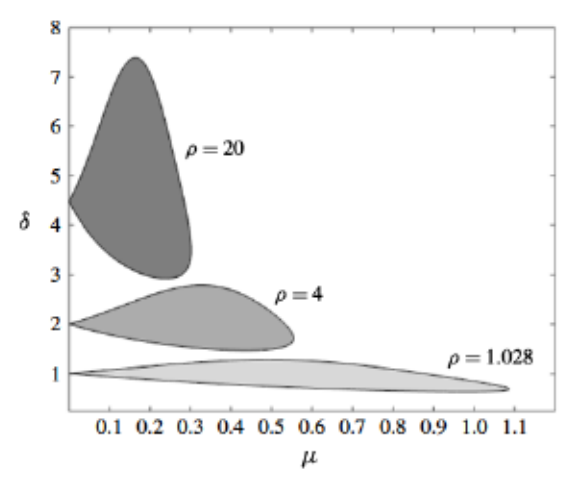


FIGURE 5. For the irrotational case ($\omega_1 = \omega_2 = 0$), regions where c_2 is negative as a function of μ and δ for discrete ρ values ranging from $\rho = 1.028$ to $\rho = 20$. The boundaries indicate parameter configurations for which $c_2 = 0$, and the interior corresponds to $c_2 < 0$.

to figure 2, the choice of vorticities corresponds to a negative value of c_2 . This is corroborated by the speed-amplitude curve in figure 6(a), which shows the speed of the wave decreasing with the increase in the amplitude.

3.5.2. Stagnation point in the upper fluid

To look at an example in which we bifurcate from a flat surface with a stagnation point in the lower fluid, we choose $\omega_1 = \omega_2 = -1$. As can be seen by examining

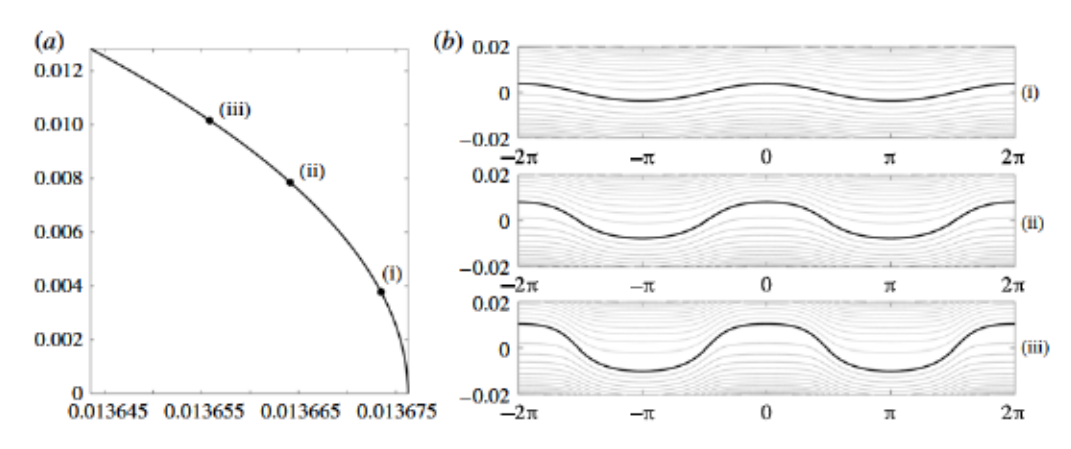


FIGURE 6. Case for $\mu = \sqrt{0.1}$, $\rho = 1.028$, $\delta = 4$, $\omega_1 = 1$ and $\omega_2 = -1$, with amplitude-speed relationship in (a) and streamlines corresponding to increasing wave amplitudes (b).

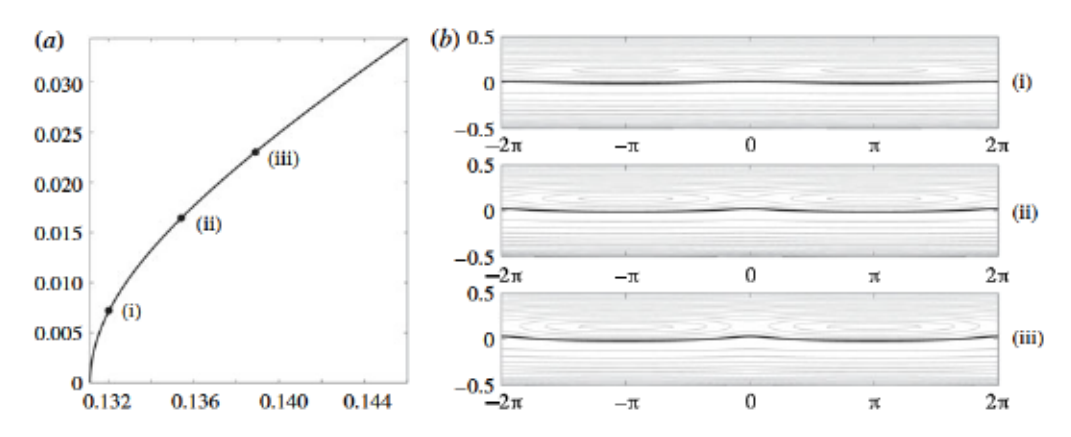


FIGURE 7. Case for $\mu = \sqrt{0.1}$, $\rho = 1.028$, $\delta = 4$, $\omega_1 = -1$ and $\omega_2 = -1$, with amplitude-speed relationship in (a) and streamlines corresponding to increasing wave amplitudes (b). The stagnation point in the upper fluid region is seen at the saddle centred around x = 0 as well as at the centres located at $x = \pm \pi$.

the interface profiles in figure 7(a), the particular case we have chosen corresponds to interfaces of elevation. By examining the impact of the stagnation point on the streamline patterns seen in figure 7(b), we can see from where this tendency towards forming interfaces of elevation comes.

3.5.3. Stagnation point in the bottom fluid

To look at an example in which we bifurcate from a flat surface with a stagnation point in the lower fluid, we choose $\omega_1 = \omega_2 = 1$. As can be seen by examining the interface profiles in figure 8(a), the particular case we have chosen corresponds to interfaces of depression. By examining the impact of the stagnation point on the streamline patterns seen in figure 8(b), we can see from where this tendency towards forming interfaces of depression comes.

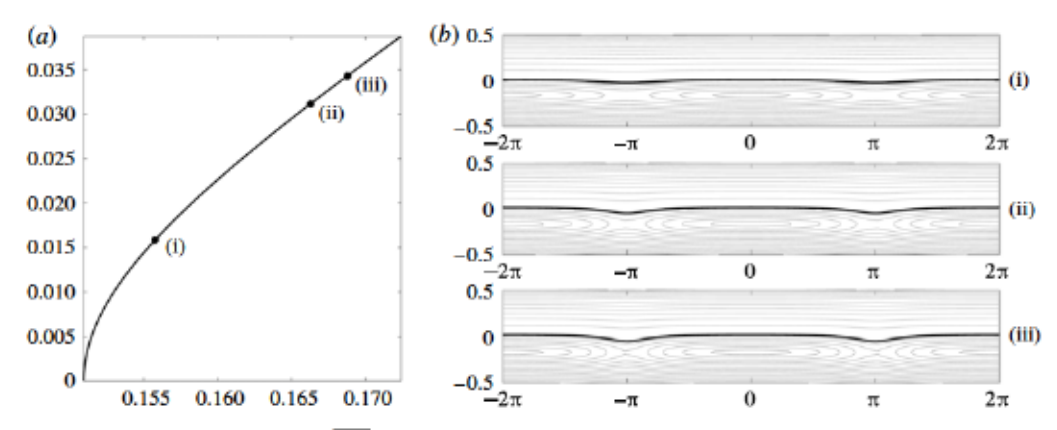


FIGURE 8. Case for $\mu = \sqrt{0.1}$, $\rho = 1.028$, $\delta = 4$, $\omega_1 = 1$ and $\omega_2 = 1$, with amplitude–speed relationship in (a) and streamlines corresponding to increasing wave amplitudes (b). The stagnation point in the lower fluid region is seen at the saddles centred around $x = \pm \pi$ and the centre located at x = 0.

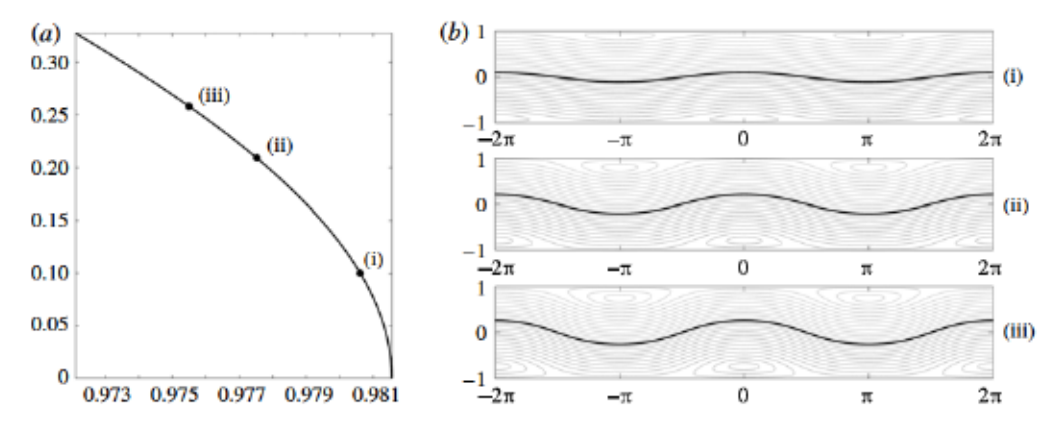


FIGURE 9. Case for $\delta = 1$, $\omega_1 = -1$, $\omega_2 = 1$, $\rho = 1.028$, with amplitude–speed relationship (a) and streamlines corresponding to increasing wave amplitudes (b). Stagnation points are showing in both the upper and lower fluids centred at x = 0 in the lower fluid, and $x = \pm \pi$ in the upper fluid.

3.5.4. Stagnation point in both fluids

To see an example in which we bifurcate with stagnation points in both the lower and upper fluid regions, we choose $\omega_1 = -1$ and $\omega_2 = 1$. In this case, we see that the tendency is for waves of depression to form which increase in speed with amplitude; see figure 9(b). The role of stagnation becomes increasingly more relevant on the nonlinear profile as its amplitude is increased, and thus has an ever increasing effect on the shape of the wave profile; compare figures 9(bii) and 9(biii). For lower amplitudes, the presence of stagnation points both above and below the interface allows for the kind of ambiguity between the interface being elevated or depressed for which the case of no stagnation points in the fluid allowed. However, the presence of stagnation points allows for the formation of broader rising portions of heavier fluid, which at larger amplitudes arguably makes the interface one of depression with sharper falling peaks that are shaped by having to move between the stagnation points in the fluid.

4. Stability formulation

We investigate the spectral stability of the travelling wave profiles computed in the previous section with respect to infinitesimal perturbations. First, it is important that we discuss what perturbations we wish to allow. It may appear natural to consider disturbances of the same period as the underlying stationary wave, as is often done in the literature. However, we wish to work with a more general class of disturbances; namely, we choose to include all bounded on the whole real line. It is important to realize that this class is the largest class of perturbations allowed by the physical problem at hand. Indeed, disturbances should be bounded and continuous functions, but there is no physical reason to restrict their spatial dependence to be periodic.

4.1. Stability formulation: problem reformulation

In order to investigate the stability of the travelling wave profiles with respect to such perturbations, it is necessary to reformulate the governing equations. Equation (2.22) is a local statement and does not require modification. However, (2.23) and (2.24) are non-local and in their current incarnation, apply specifically to waves of period L. Thus, we cannot use the equation in its current form for any bounded function on the real line.

Following the method outlined in Deconinck & Oliveras (2011), we reformulate the non-local equations on the whole line via a spatial average value. For a continuous bounded function f(x), i.e. $f \in C_b^0(\mathbb{R})$, let $\langle f \rangle$ represent the spatial average of the function defined by

$$\langle f \rangle = \lim_{M \to \infty} \frac{1}{M} \int_{-M/2}^{M/2} f(x) \, \mathrm{d}x. \tag{4.1}$$

It should be noted that the kernel of this operation is quite large. For instance, all functions that approach zero as $|x| \to \infty$ have zero spatial average. Nevertheless, we may use the spatial average to replace (2.23) and (2.24) with the more general non-local equations given by

$$\langle e^{-ikx}((ik\epsilon \mu^2 \partial_t \eta - \omega_1)C_1 - \mu k(\epsilon(\partial_x q_1 - \omega_1 \eta) - c)S_1)\rangle = 0,$$
 (4.2)

and

$$\langle e^{-ikx}((ik\epsilon \mu^2 \partial_t \eta - \omega_2)C_2 - \mu k(\epsilon(\partial_x q_2 - \omega_2 \eta) - c)S_2)\rangle = 0,$$
 (4.3)

where S_j and C_j are defined as before. These equations are valid for all $k \in \mathbb{R}_0 = \mathbb{R} - \{0\}$, as no quantization condition is imposed by the periodicity of the solutions considered. Further, as solutions of increasingly larger period are considered, the set of k values to be considered in (4.2) and (4.3) approaches a dense subset of the real line. The equation corresponding to k = 0 is excluded, as before. Equations (4.2) and (4.3) allow us to perturb our travelling wave solution with any bounded perturbation regardless of periodicity.

4.2. Stability formulation: eigenvalue problem

Having generalized the dynamical equations to accommodate the perturbations we wish to consider, we briefly discuss the definition of spectral stability. A stationary solution of a nonlinear problem is spectrally stable if there are no exponentially growing modes of the corresponding linearized problem. To determine the spectral stability of the periodic travelling wave solutions, we start by considering a travelling

wave solution set $(\eta_0(x-ct), \alpha_0(x-ct), \beta_0(x-ct))$. In the same travelling coordinate frame, we add a small perturbation of the form

$$\eta(x - ct, t) = \eta_0(x - ct) + \varepsilon \eta_1(x - ct)e^{\lambda t} + O(\varepsilon^2), \tag{4.4}$$

$$q_1(x - ct, t) = \alpha_0(x - ct) + \varepsilon \alpha_1(x - ct)e^{\lambda t} + O(\varepsilon^2), \tag{4.5}$$

$$q_2(x - ct, t) = \beta_0(x - ct) + \varepsilon \beta_1(x - ct)e^{\lambda t} + O(\varepsilon^2), \tag{4.6}$$

where ε is a small parameter. The perturbations η_1 , α_1 and β_1 are moving at the same speed and in the same direction as the original travelling wave solution. Our goal is to determine the time dependence of the perturbation in order to determine how the deviation from the unperturbed solution evolves.

As we are linearizing about a travelling wave solution, we substitute the above expansions for q_1 , q_2 and η into (2.22), (4.2) and (4.3) keeping only $O(\varepsilon)$ terms. This is rewritten compactly as

$$\lambda \mathcal{L}_1 U(x) = \mathcal{L}_2 U(x), \tag{4.7}$$

where \mathcal{L}_1 and \mathcal{L}_2 are 3×3 matrices of linear operators and U(x) is a vector-valued function with entries $U(x) = [\eta_1 \alpha_1 \beta_1]^T$. Details are provided in appendix A.

Since the time dependence of the perturbation depends exponentially on λ , we can determine information about the stability of the underlying travelling wave by determining all bounded solutions of this generalized eigenvalue problem. If any bounded solutions U(x) exist for which the corresponding λ has a positive real part, the linear approximation of the solution will grow in time and thus the perturbed solution will exponentially diverge from the stationary solution in the linear approximation.

Since the coefficient functions of (4.7) are periodic in x with period 2π , we decompose the perturbations further using Floquet's theorem (see Deconinck & Kutz 2006; Curtis & Deconinck 2010). This allows us to further decompose η_1 , α_1 and β_1 in the form

$$\eta_1(x) = e^{ipx} \bar{\eta}_1(x), \quad \alpha_1(x) = e^{ipx} \bar{\alpha}_1(x), \quad \beta_1(x) = e^{ipx} \bar{\beta}_1(x), \quad (4.8a-c)$$

where $\bar{\eta}_1(x)$, $\bar{\alpha}_1$ and $\bar{\beta}_1$ are periodic with period 2π and p (the Floquet exponent) can be restricted to the interval [-1/2, 1/2].

Substituting the Floquet decomposition directly into (4.7) while simultaneously using the Fourier series representation for $\bar{\eta}_0$, $\bar{\alpha}_0$ and $\bar{\beta}_0$, we obtain a new equation of the form

$$\lambda \tilde{\mathcal{L}}_1(p)\hat{U} = \tilde{\mathcal{L}}_2(p)\hat{U},$$
 (4.9)

where \hat{U} represents the concatenation of three bi-infinite vectors of the Fourier coefficients for $\bar{\eta}_1$, $\bar{\alpha}_1$ and $\bar{\beta}_1$. For $j=1,\,2,\,\tilde{\mathcal{L}}_j(p)$ are linear operators that now depend on the Floquet exponent p. Equation (4.9) gives a generalized bi-infinite eigenvalue problem for determining the spectrum of the linearized operator about the stationary travelling wave solutions.

Instead of directly solving the eigenvalue problem as stated above, a more stable approach is to reformulate the problem as a quadratic eigenvalue problem for the eigenvalue λ and the corresponding eigenfunction $\bar{\eta}_1$ of the form

$$(\lambda^2 A_2(p) + \lambda A_1(p) + A_0(p))\bar{\eta}_1 = 0.$$
 (4.10)

Details regarding (4.10), the form of the A_j values for j = 0, 1 and 2 are given in appendix B.

We solve this generalized eigenvalue problem numerically by truncating the Fourier series representation for $\bar{\eta}_1$ over $\mathbb{Z} - \{0\}$ to $\{\pm 1, \pm 2, \ldots, \pm N\}$ where we have eliminated the zero mode as we only consider zero-average perturbations to the free surface. With this truncation, we obtain 2N quadratic equations for 2N unknown Fourier coefficients of $\bar{\eta}_1$. Finally, we note that due to the underlying symmetries in the problem, we may restrict the p interval from [-1/2, 1/2] to [0, 1/2] and consider both λ and the conjugate of λ . Thus, for every $p \in [0, 1/2]$, we solve the generalized eigenvalue problem given by

$$(\lambda^2 A_2^{(N)}(p) + \lambda A_1^{(N)}(p) + A_0^{(N)}(p))\hat{\eta}_1^{(N)} = 0,$$
 (4.11)

where the superscript (N) denotes the projection onto the N Fourier modes. This is done via the QZ algorithm (Moler & Stewart 1973). The dimension of the truncation on the Fourier modes is chosen so that both the eigenvalues and eigenvectors converge to 12 digits of accuracy.

5. Stability results

Using the formulation outlined in the previous section, we numerically compute spectra beginning with irrotational interfacial waves. It is well known that the trivial solution is subject to the Kelvin–Helmholtz instability provided that there is a jump in the horizontal velocity at the interface. However, the role that nonlinearities play in the formation of possible Kelvin–Helmholtz instabilities in our configuration is not as well known. In what follows then, we examine the role nonlinearity plays in the formation of instabilities by examining the spectra associated with the non-trivial TWSs presented in the previous section. We begin by considering the spectral stability corresponding to the irrotational problem and then subsequently explore the impact of linear shear.

Remark 4. Before we proceed to the general results, it is important to note that the density of the chosen Floquet parameters p is critical for drawing the correct stability/instability conclusions. As outlined in the previous section, we should calculate the above quadratic eigenvalue problem for all p values in the interval [-1/2, 1/2). For example, if a uniform grid of p values is chosen, any concerns about missing isolated stability phenomena can be resolved by choosing a finer resolution of p values. However, the numerical resolution required becomes intractable as the underlying TWS become more nonlinear. Instead, we chose to work with a non-uniform set of p values using the Hamiltonian structure of the problem (see McLean 1982a,b; Francius & Kharif 2006; Deconinck & Oliveras 2011). These ideas rely on knowing the Krein signature of the eigenvalues for the trivial solution. See appendix C for the Hamiltonian formulation and computation of the Krein signatures.

For each branch of travelling wave solutions, we determine the Floquet parameters that give rise to the collisions of eigenvalues with opposite signatures. We concentrate a locally dense mesh of Floquet parameters about each of these parameter values in addition to a uniform spacing of p values throughout the interval. As we consider the stability of non-trivial solutions, we refine and adapt our mesh of Floquet parameters to track instabilities.

It is straightforward to show that the trivial solution will be spectrally stable when there is no jump in the tangential velocity at the interface. However, the spectral stability is not guaranteed for non-trivial solutions that bifurcate from this

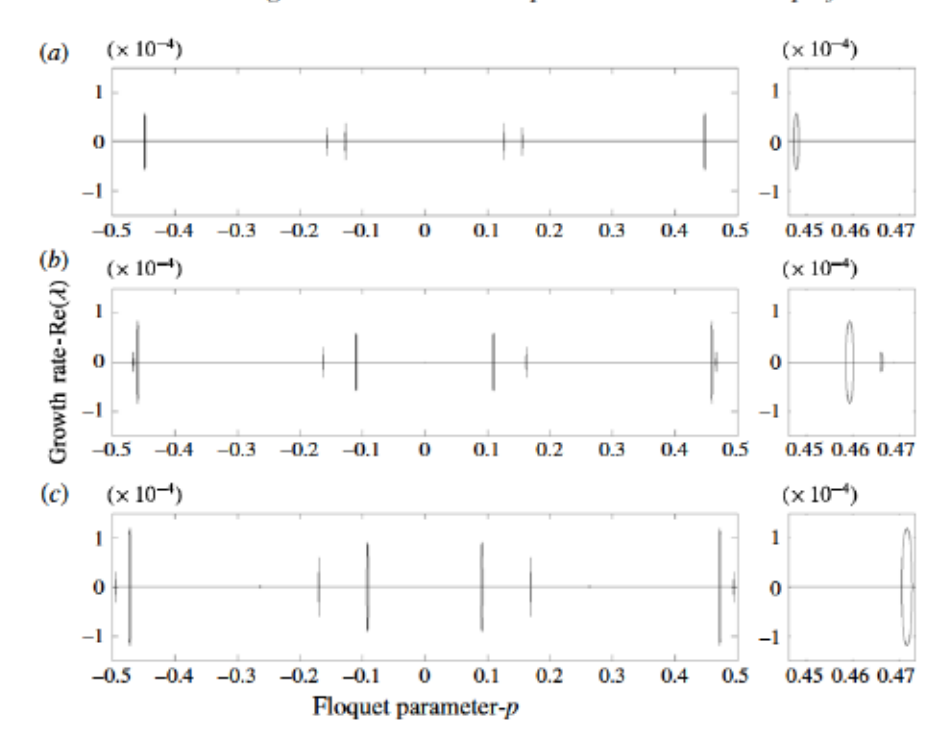


FIGURE 10. Real part of growth rates as a function of the Floquet parameter p with $\omega_1 = \omega_2 = 0$, $\rho = 1.028$, $\delta = 4$, $\mu = \sqrt{0.1}$ and ϵ increasing from $\epsilon \approx 0.16$ (a), $\epsilon \approx 0.18$ (b) and $\epsilon \approx 0.2$. The right panel is a zoomed-in version of a region in the left panel and demonstrates that the spikes seen on the left do indeed represent continuous curves in the Floquet parameter. While narrow bands of HFIs are clearly visible, the absence of spectra near $p \sim 0$ shows MIs are not present.

solution. Throughout this section, we consider two separate classes of instabilities: modulational instabilities (MIs) corresponding to Floquet parameter $p \sim 0$ with λ in an ϵ neighbourhood of the origin, and high-frequency instabilities (HFIs) corresponding to the Floquet parameter $p \gg 0$. It is worth noting that the HFIs are a result of collisions of eigenvalues not resulting for p=0. While computations need only be done for Floquet parameters $p \in [0, 1/2]$ due to underlying symmetries in the problem, we plot spectra over $p \in [-1, 1]$ for illustrative purposes.

For the configuration with $\mu = \sqrt{0.1}$, $\epsilon = 0.1$ and $\rho = 1.028$, figure 10 shows the maximum growth rate as a function of the Floquet parameter p for increasing values of the amplitude of the travelling wave solution η . As in the single-layer free-boundary problem, all non-zero, small-amplitude travelling waves appear unstable to perturbations corresponding to HFIs localized around small bands of Floquet parameters p. An interesting finding is that for the various depth ratios examined in the irrotational problem with fixed $\mu = \sqrt{0.1}$, all solutions are not susceptible to MIs. However, if μ and δ are varied appropriately, then even the irrotational problem may become susceptible to both HFI and MI. For example, as seen in figure 11, when $\mu = \delta = 2$, $\rho = 1.028$, travelling wave solutions are susceptible to both HFIs and MIs where magnitude of both instabilities increase as a function of increasing ϵ .

Including vorticity has an impact on the strength of HFI as seen in figure 12, thereby adding a mechanism for the suppression of instability not seen in the stratified

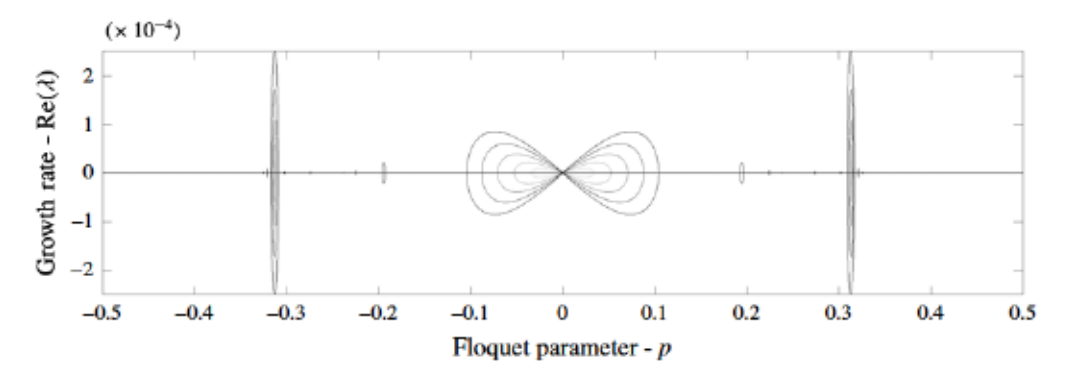


FIGURE 11. Real part of growth rates as a function of the Floquet parameter p with $\omega_1 = \omega_2 = 0$, $\rho = 1.028$, $\delta = 2$, $\mu = 2$ and ϵ increasing from $\epsilon \approx 0.001$ (light grey) to $\epsilon \approx 0.08$ (darker grey). Both MI and HFI are present in this scenario.

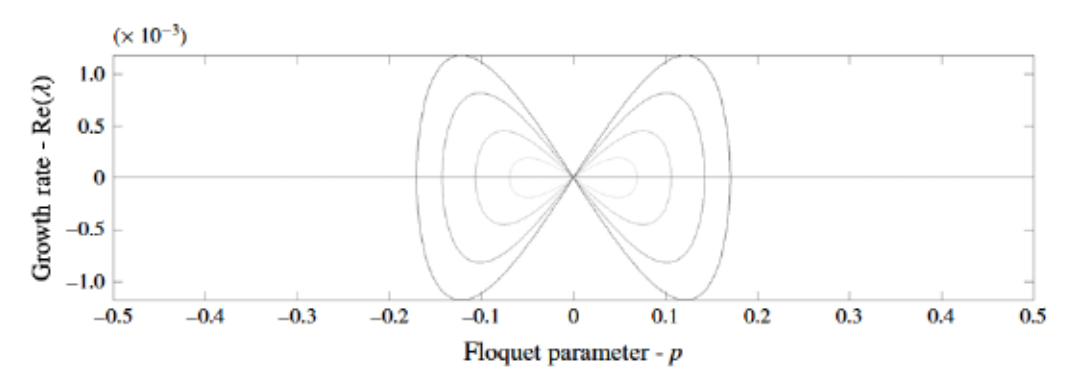


FIGURE 12. Real part of growth rates as a function of the Floquet parameter p with $\omega_1=-1$, $\omega_2=1$, $\rho=1.028$, $\delta=2$, $\mu=2$ and ϵ increasing from $\epsilon\approx0.001$ to $\epsilon\approx0.08$. While the MI instabilities are present, the magnitudes of the HFIs have been significantly diminished due to the presence of the shear in both layers.

shear-free case. Furthermore, the inclusion of vorticity may also impact whether or not a travelling wave is susceptible to MI. This hints at the more complicated role that vorticity plays in understanding and parameterizing regions of instability for the various parameters in the problem.

We explore this issue more fully in figures 13 and 14. Here, we show how different balances between the shear, depth ratio and μ either allow or suppress MIs. For simplicity, in figure 13, we have chosen $\mu = \delta$. While this particular choice is unnecessary, not choosing so further expands the possible parameter space to be explored. In fixing either ω_1 or ω_2 to be zero, we can see how the threshold between δ and the strength of the shear must be related in order from small-amplitude travelling wave solutions to be susceptible to MI. Figure 14 shows how this relationship becomes more complicated as both ω_1 and ω_2 are simultaneously varied when $\mu = \delta = 2$. We note that we do not find MI for example when $\mu = \sqrt{0.1}$ using the solutions presented in § 3 (see figures 15–17). Whether this is a general feature for all solutions, and what the exact parameter values are which ensure the existence of MIs, is a subject of future study. We do show that the growth rates, and bands of

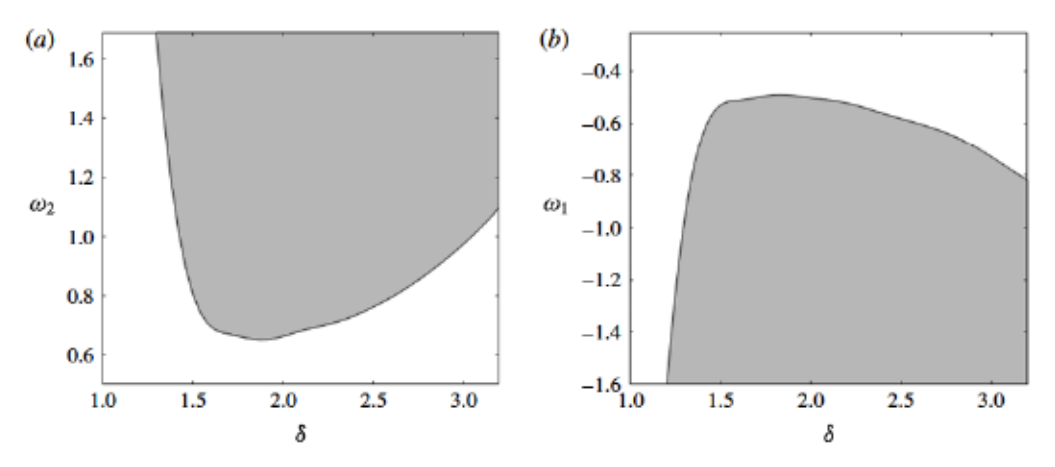


FIGURE 13. Region of MIs (shaded) as a function of δ for small-amplitude solutions with $\rho = 1.028$ and $\mu = \delta$. (a) The value of ω_1 is fixed to be zero while the value of ω_2 is varied. (b) The value of ω_2 is fixed to be zero while the value of ω_1 is varied.

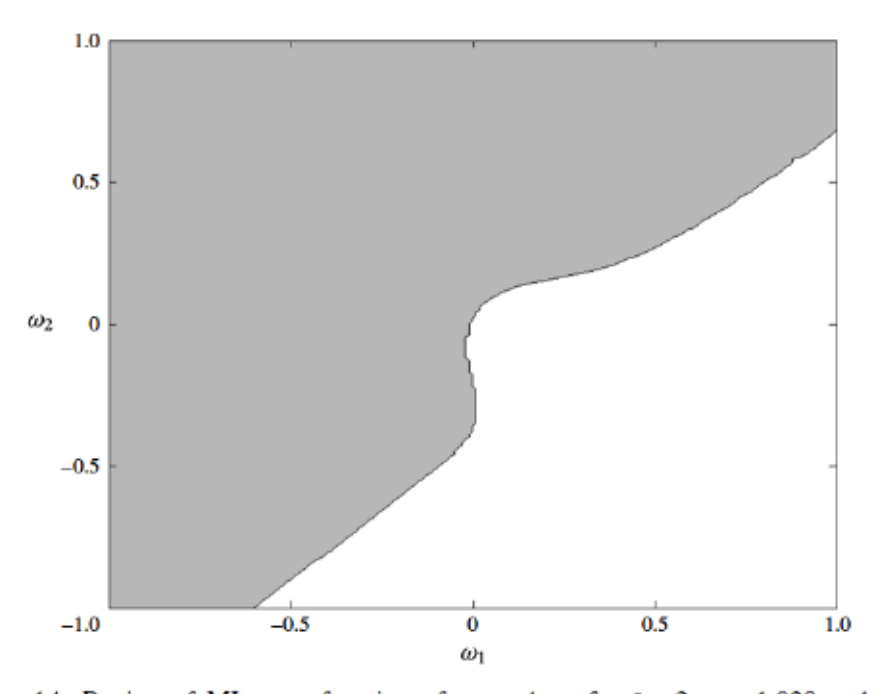


FIGURE 14. Region of MIs as a function of ω_1 and ω_2 for $\delta = 2$, $\rho = 1.028$ and $\mu = 2$.

instability corresponding to m=2, m=3 and m=4 resonant interactions grow at rates proportional to ϵ^2 , ϵ^3 , and ϵ^4 as demonstrated in figure 18.

When limited to the irrotational case ($\omega_1 = \omega_2 = 0$), our results appear in good qualitative agreement with the experimental results presented in Grue *et al.* (1999). Specifically, as noted in their work when $\delta = 4$, instabilities do not appear detectible except for large-amplitude waves. Given the time scales involved in their experiment, this appears consistent with the HFIs (see figure 10) being undetectable. Further

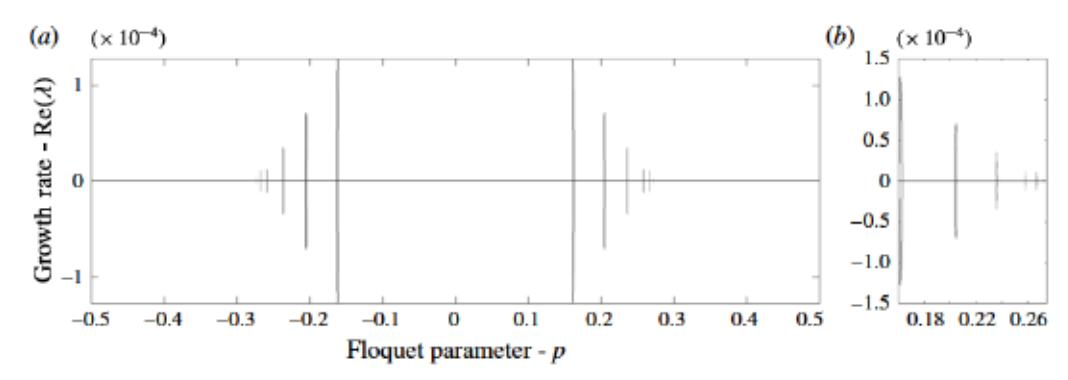


FIGURE 15. Real part of growth rates as a function of the Floquet parameter p with $\omega_1 = -1$, $\omega_2 = 1$, $\rho = 1.028$, $\delta = 1$, $\mu = \sqrt{0.1}$ and ϵ increasing from $\epsilon \approx 0.001$ (light grey) to $\epsilon \approx 0.25$ (darker grey). (b) Zoomed-in version of a region in (a) demonstrating that the spikes seen on the left do indeed represent continuous curves in the Floquet parameter. As the amplitude increases, the Floquet parameter associated with the dominant instability decreases.

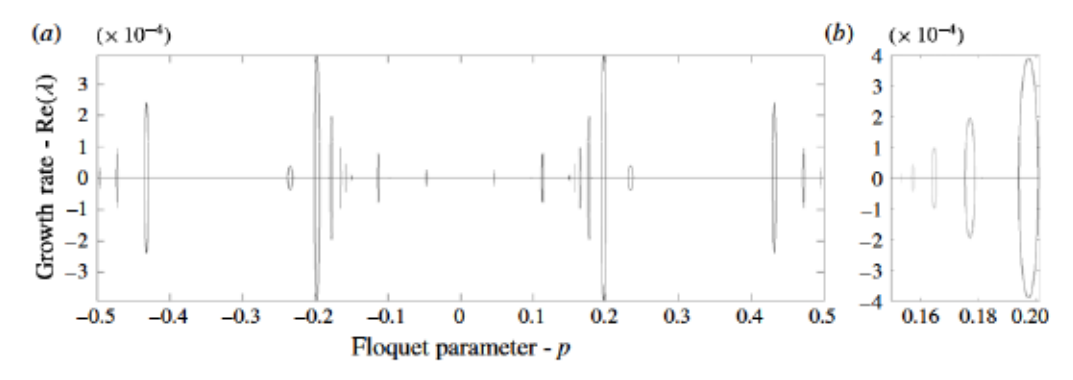


FIGURE 16. Real part of growth rates as a function of the Floquet parameter p with $\omega_1 = 1$, $\omega_2 = 1$, $\rho = 1.028$, $\delta = 4$, $\mu = \sqrt{0.1}$ and ϵ increasing from $\epsilon \approx 0.001$ (light grey) to $\epsilon \approx 0.015$ (darker grey). (b) Zoomed-in version of a region in (a) demonstrating that the spikes seen on the left do indeed represent continuous curves in the Floquet parameter. As the amplitude increases, the Floquet parameter associated with the dominant instability increases.

investigation is clearly warranted, and we aim to compare more carefully in future work.

We note that these results generalize the behaviour of both MIs and HFIs in the irrotational case. These results also expand on those for a single-layer fluid, where the strength of the linear shear has a dramatic effect on the instability of TWSs as discussed in Thomas *et al.* (2012) for approximate models, and in Oliveras *et al.* (2016) for the full water-wave problem.

6. Concluding remarks

Although we focused on internal waves limited to a one-dimensional interface represented by a graph, we can easily adapt our problem formulation to an arclength

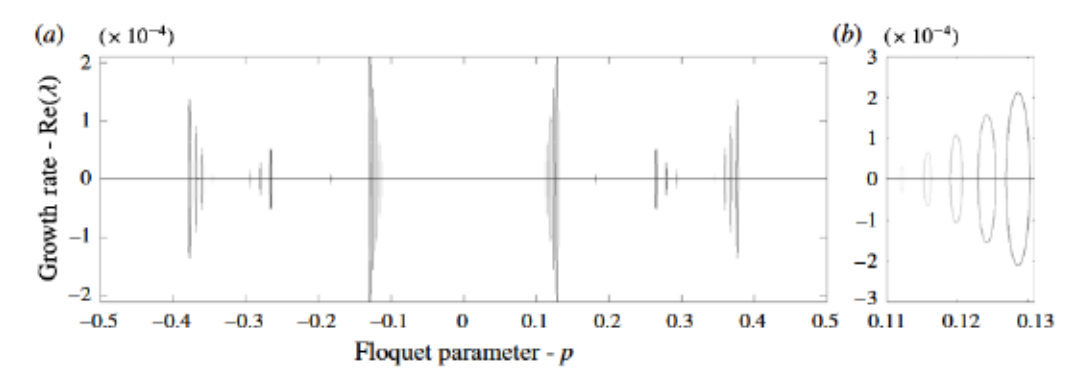


FIGURE 17. Real part of growth rates as a function of the Floquet parameter p with $\omega_1 = -1$, $\omega_2 = -1$, $\rho = 1.028$, $\delta = 4$, $\mu = \sqrt{0.1}$ and ϵ increasing from $\epsilon \approx 0.001$ (light grey) to $\epsilon \approx 0.03$ (darker grey). (b) Zoomed-in version of a region in (a) demonstrating that the spikes seen on the left do indeed represent continuous curves in the Floquet parameter. As the amplitude increases, the Floquet parameter associated with the dominant instability increases.

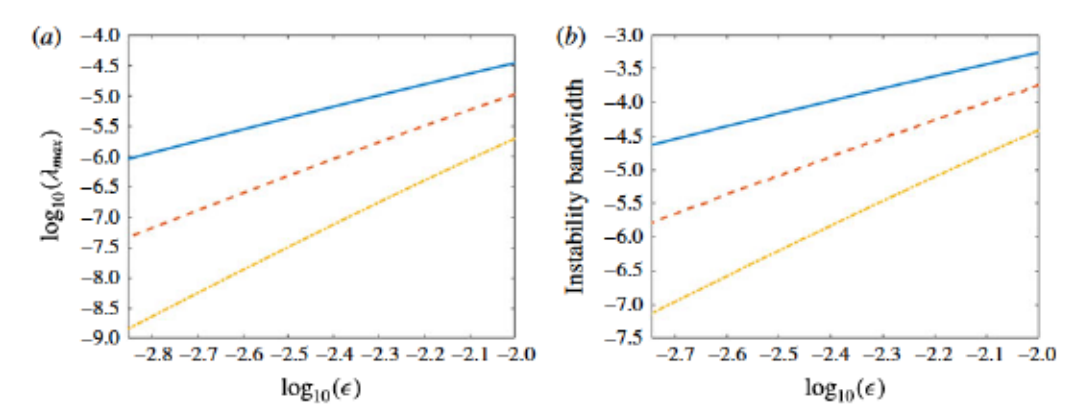


FIGURE 18. (Colour online) The bifurcation curves for the maximum growth rate (a) and instability bandwidth (b) as a function of amplitude corresponding to m = 2 (solid), m = 3 (dashed) and m = 4 (dash-dot) as defined in appendix C. Here, $\omega_1 = -1$, $\omega_2 = -1$, $\rho = 1.028$, $\delta = 4$, $\mu = \sqrt{0.1}$.

parametric representation (see Ashton & Fokas 2011; Akers *et al.* 2016). Overturning waves, as well as the Hamiltonian structure of our will be explored in a future paper. Despite our focus on single-valued waves, we show a variety of solution structures depending on the density and depth ratios yielding waves of elevation or depression as characterized by the sign of c_2 in our formulation. This is directly related to the second-order correction of the tangent angle of the interface as prescribed by the vortex-sheet formulation of the interface for irrotational fluids over infinite depth in Akers *et al.* (2016). Here, we have extended these results to finite depth and linear shear.

For the single-valued solutions, we show that internal waves can be stabilized by the strength of the linear shear in each layer. While one can amplify the instabilities seen in figure 12, the modulational instabilities can be fully suppressed to machine precision if the differences in magnitudes of the depths of the stratified layers is large enough (see figure 13 for details). This extends the work in Pullin & Grimshaw (1986) where they focus on modulational instabilities on fluids of infinite depth and limit their investigates on HFI to that of m=2 resonant interaction. Here, we consider all resonant interactions that give rise to a growth rate with real part >10⁻¹⁴. We show that in finite depth, the combination of shears in each layer that gives rise to modulational instability varies significantly from the infinite-depth scenario (Pullin & Grimshaw 1986). The region of stability for the finite-depth case presented in figure 14 contains a significantly larger portion fourth quadrant of the (ω_1, ω_2) plane as well as regions of the first and third quadrant. For infinite depth, this stability region is shown to be much smaller, and limited to the fourth quadrant only (Pullin & Grimshaw 1986).

This ability of shear to both amplify and suppress modulational stability in bistratified fluids generalizes the phenomena seen for the single-layer fluid where modulational instabilities are suppressed provided that the strength of the vorticity exceeds a critical threshold (see Thomas *et al.* 2012; Oliveras *et al.* 2016).

We also see that the modulational instability is not necessarily the dominant instability when present. Indeed, for small-amplitude waves, the growth rate of the HFI may be the same as those of the MI such as what is shown in figure 11. Furthermore, the dominant instabilities corresponding to resonant interactions can either increase (see figure 16), decrease (see figure 15), or remain stationary (see figure 11) in Floquet parameter as the amplitude of the underlying travelling wave solution increases or decreases depending on the order of the resonant interaction as well as the parameters involved.

Acknowledgements

This work was completed at the Institute for Computational and Experimental Research in Mathematics (ICERM) in Providence, RI. Both K.L.O. and C.W.C. gratefully acknowledge the support of ICERM and their computing facilities. K.L.O. also acknowledges the support of the National Science Foundation under grant number DMS-1313049 and DMS-1715082. C.W.C. acknowledges support of the National Science Foundation under grant number DMS-1715039. Any opinions, findings, and conclusions or recommendations expressed in this material are those of the authors and do not necessarily reflect the views of the National Science Foundation.

Appendix A. Stability formulation

For simplicity, we replace x - ct with x where the non-dimensional variables η and q_j (j = 1, 2) are periodic in the new variable x with period 2π . Substituting the expansions for η , q_1 and q_2 into (2.22), we find at $O(\varepsilon)$

$$V\eta_{1}(x) - T_{1}\partial_{x}\alpha_{1}(x) + T_{2}\partial_{x}\beta_{1}(x) = \lambda((-\tilde{\omega}\partial_{x}^{-1} - (T_{1} - T_{2})(\partial_{x}\eta_{0}))\eta_{1}(x) + \alpha_{1}(x) - \rho\beta_{1}(x)),$$
 (A 1)

where

$$V = \left((\rho - 1) + \omega_1 T_1 - \omega_2 T_2 + \epsilon \mu^2 \epsilon \mu^2 (\partial_x \eta_0) \left(T_1^2 - \frac{1}{\rho} T_2^2 \right) \partial_x \right),$$

$$\tilde{\omega} = \omega_1 - \rho \omega_2, \quad T_1 = \frac{(\epsilon \alpha_0(x) - \omega_1 \epsilon \eta_0(x) - c)}{1 + \epsilon^2 \mu^2 (\partial_x \eta_0)^2}, \quad \text{and}$$

$$T_2 = \frac{\rho(\epsilon \beta_0(x) - \omega_2 \epsilon \eta_0(x) - c)}{1 + \epsilon^2 \mu^2 (\partial_x \eta_0)^2}.$$
(A 2)

For the non-local equations given by (4.2), and (4.3), we find

$$\begin{split} \lambda \langle \mathrm{e}^{-\mathrm{i}kx} \mathcal{C}_{1,k} \eta_1(x) \rangle \\ &= \langle \mathrm{e}^{-\mathrm{i}kx} (-\mathrm{i}k \mathcal{C}_{1,k} (\epsilon(\partial_x \alpha_0) - \omega_1 \epsilon \eta_0 - c) \eta_1(x)) \rangle - \frac{\mathrm{i}}{\mu} \langle \mathrm{e}^{-\mathrm{i}kx} (\mathcal{S}_{1,k} \partial_x \alpha_1(x)) \rangle, \qquad (\mathrm{A} \, 3) \\ \lambda \langle \mathrm{e}^{-\mathrm{i}kx} \mathcal{C}_{2,k} \eta_1(x) \rangle \\ &= \langle \mathrm{e}^{-\mathrm{i}kx} (-\mathrm{i}k \mathcal{C}_{2,k} (\epsilon(\partial_x \beta_0) - \omega_2 \epsilon \eta_0(x) - c) \eta_1(x)) \rangle - \frac{\mathrm{i}}{\mu} \langle \mathrm{e}^{-\mathrm{i}kx} (\mathcal{S}_{2,k} \partial_x \beta_1(x)) \rangle. \quad (\mathrm{A} \, 4) \end{split}$$

Appendix B. Generalized matrix eigenvalue problem

Since $\bar{\alpha}_1$, $\bar{\beta}_1$ and $\bar{\eta}_1$ are 2π periodic, we can represent the functions by their Fourier Series given by

$$\bar{\alpha}_1(x) = \sum_{n=-\infty}^{\infty} e^{in\pi x} \hat{A}_n, \quad \bar{\beta}_1(x) = \sum_{n=-\infty}^{\infty} e^{in\pi x} \hat{B}_n, \quad \bar{\eta}_1(x) = \sum_{n=-\infty}^{\infty} e^{in\pi x} \hat{N}_n. \quad (B \ 1a - c)$$

Following the steps outlined in § 4, the resulting eigenvalue problem takes the for

$$\begin{bmatrix} \mathcal{L}_{1,1} & \mathcal{L}_{1,2} & \mathcal{L}_{1,3} \\ \mathcal{L}_{2,1} & \mathcal{L}_{2,2} & 0 \\ \mathcal{L}_{3,1} & 0 & \mathcal{L}_{3,3} \end{bmatrix} X = \lambda \begin{bmatrix} \mathcal{R}_{1,1} & \mathcal{R}_{1,2} & \mathcal{R}_{1,3} \\ \mathcal{R}_{2,1} & 0 & 0 \\ \mathcal{R}_{3,1} & 0 & 0 \end{bmatrix} X,$$
 (B 2)

where

$$\mathcal{L}_{1,1} = \left((\rho - 1) + \omega_1 T_1 - \omega_2 T_2 - \epsilon \mu (\partial_x \eta_0) \left(\frac{1}{\rho} T_2^2 - T_1^2 \right) \partial_x \right), \quad \mathcal{L}_{1,2} = -T_1 \partial_x,$$

$$\mathcal{L}_{1,3} = T_2 \partial_x, \quad \mathcal{L}_{2,1}(k) = k(\epsilon (\partial_x \alpha_0) - \epsilon \omega_1 \eta_0(x) - c) \cosh(\mu k(\epsilon \eta_0 - 1)),$$

$$\mathcal{L}_{2,2}(k) = \frac{1}{\mu} \sinh(\mu k(\epsilon \eta_0 - 1)) \partial_x,$$

$$\mathcal{L}_{3,1}(k) = k(\epsilon (\partial_x \beta_0) - \epsilon \omega_2 \eta_0(x) - c) \cosh(\mu k(\epsilon \eta_0 + \delta)),$$

$$\mathcal{L}_{3,3}(k) = \frac{1}{\mu} \sinh(\mu k(\epsilon \eta_0 + \delta)) \partial_x,$$
(B 3)

and

$$\mathcal{R}_{1,1} = \tilde{\omega} \partial_x^{-1} + (T_1 - T_2)(\partial_x \eta_0), \quad \mathcal{R}_{1,2} = 1, \quad \mathcal{R}_{1,3} = -\rho, \\
\mathcal{R}_{2,1}(k) = i \cosh(\mu k (\epsilon \eta_0 - 1)), \quad \mathcal{R}_{3,1}(k) = i \cosh(\mu k (\epsilon \eta_0 + \delta)),$$
(B 4)

where $k = p + \ell$, for $\ell \in \mathbb{Z}$, and $X = e^{i\mu x} [\bar{\eta}_1 \bar{\alpha}_1 \bar{\beta}_1]^T$.

Instead of directly solving the eigenvalue problem as stated above, a more stable approach is to calculate the eigenvalues is to reformulate the problem as a quadratic eigenvalue problem. Noting that both $\mathcal{L}_{2,2}$ and $\mathcal{L}_{3,3}$ are invertible (see Craig *et al.* 2005b), we can formally replace both $\bar{\alpha}_1$ and $\bar{\beta}_1$ with the expressions

$$\bar{\alpha}_1 = \mathcal{L}_{2,2}^{-1}(\lambda \mathcal{R}_{2,1} - \mathcal{L}_{2,1})\bar{\eta}_1, \quad \bar{\beta}_1 = \mathcal{L}_{3,3}^{-1}(\lambda \mathcal{R}_{3,1} - \mathcal{L}_{3,1})\bar{\eta}_1. \tag{B 5a,b}$$

Using these expressions in the 3×3 eigenvalue problem above, we can reduce the system to a quadratic eigenvalue problem of the form

$$(\lambda^2 A_2 + \lambda A_1 + A_0)\bar{\eta}_1 = 0,$$
 (B 6)

where the expressions for the operators A_i are given by

$$A_0 = \mathcal{L}_{1,1} - \mathcal{L}_{1,2} \mathcal{L}_{2,2}^{-1} \mathcal{L}_{2,1} - \mathcal{L}_{1,3} \mathcal{L}_{3,3}^{-1} \mathcal{L}_{3,1}, \tag{B7}$$

$$\mathcal{A}_{1} = -\mathcal{R}_{1,1} + \mathcal{R}_{1,2}\mathcal{L}_{2,2}^{-1}\mathcal{L}_{2,1} + \mathcal{L}_{1,2}\mathcal{L}_{2,2}\mathcal{R}_{2,1} + \mathcal{L}_{1,2}\mathcal{L}_{3,3}^{-1}\mathcal{R}_{3,1} + \mathcal{R}_{1,3}\mathcal{L}_{3,3}^{-1}\mathcal{L}_{3,1}, \quad (B 8)$$

$$A_2 = -\mathcal{R}_{1,2}\mathcal{L}_{2,2}^{-1}\mathcal{R}_{2,1} - \mathcal{R}_{1,3}\mathcal{L}_{3,3}^{-1}\mathcal{R}_{3,1}. \tag{B9}$$

Appendix C. Variational structure and resonant interactions

Following the now established variational procedure first outlined in Luke (1967), we can readily verify that a Lagrangian for our two-layer fluid system with shear is given in dimensional units by

$$\mathcal{L} = -\rho_1 \int_0^{2\pi L} \int_{\eta}^{h_1} \left(\partial_t \varphi_1 + \frac{1}{2} |u_1|^2 + gz \right) dz dx + \frac{\omega_1 \rho_1}{2} \int_0^{2\pi L} \eta \partial_x^{-1} \eta_t dx -\rho_2 \int_0^{2\pi L} \int_{-h_2}^{\eta} \left(\partial_t \varphi_2 + \frac{1}{2} |u_2|^2 + gz \right) dz dx - \frac{\omega_2 \rho_2}{2} \int_0^{2\pi L} \eta \partial_x^{-1} \eta_t dx. \quad (C1)$$

Passing to surface variables, this becomes

$$\mathcal{L} = \rho_1 \int_0^{2\pi L} \left(-q_1 \partial_t \eta + \frac{1}{2} q_1 G_u(\eta) q_1 + \frac{g}{2} \eta^2 + \frac{\omega_1^2}{6} \eta^3 - \omega_1 q_1 \eta \partial_x \eta + \frac{\omega_1}{2} \eta \partial_x^{-1} \partial_t \eta \right) dx + \rho_2 \int_0^{2\pi L} \left(q_2 \partial_t \eta - \frac{1}{2} q_2 G_l(\eta) q_2 - \frac{g}{2} \eta^2 - \frac{\omega_2^2}{6} \eta^3 + \omega_2 q_2 \eta \partial_x \eta - \frac{\omega_2}{2} \eta \partial_x^{-1} \partial_t \eta \right) dx.$$
(C 2)

Collecting those terms which depend on time then gives us

$$\mathcal{L} = \int_0^{2\pi L} p \partial_t \eta \, \mathrm{d}x - H(\eta, p), \tag{C3}$$

where

$$p = \rho_2 q_2 - \rho_1 q_1 - \frac{1}{2} (\rho_2 \omega_2 - \rho_1 \omega_1) \partial_x^{-1} \eta$$
 (C4)

and the Hamiltonian H is given by

$$H = \int_{0}^{2\pi L} dx \left(\rho_{2} \left(\frac{1}{2} q_{2} G_{l}(\eta) q_{2} + \frac{g}{2} \eta^{2} + \frac{\omega_{2}^{2}}{6} \eta^{3} - \omega_{2} \eta \eta_{x} q_{2} \right) - \rho_{1} \left(\frac{1}{2} q_{1} G_{u}(\eta) q_{1} + \frac{g}{2} \eta^{2} + \frac{\omega_{1}^{2}}{6} \eta^{3} - \omega_{1} \eta \eta_{x} q_{1} \right) \right), \tag{C5}$$

where we have introduced the Dirichlet-to-Neumann operators (DNOs) $G_u(\eta)$ and $G_l(\eta)$ where

$$G_u(\eta) = -\partial_x \eta \partial_x \phi_1 + \partial_z \phi_1, \quad G_l(\eta) = -\partial_x \eta \partial_x \phi_2 + \partial_z \phi_2,$$
 (C 6a,b)

so that the kinematic conditions at the boundary are given by

$$\partial_t \eta = G_u(\eta) + \omega_1 \eta \partial_x \eta, \quad \partial_t \eta = G_l(\eta) + \omega_2 \eta \partial_x \eta.$$
 (C7a,b)

This of course is still not in terms of canonical variables alone. Following the methodology in Craig, Guyenne & Kalisch (2005a), using the kinematic conditions across the boundary, we have that

$$G_l(\eta)q_2 - \omega_2\eta \partial_x \eta = G_u(\eta)q_1 - \omega_1\eta \partial_x \eta. \tag{C8}$$

This then leads to the transformations

$$q_{1} = \tilde{G}_{11}(\eta) \left(p + \frac{1}{2} (\rho_{2}\omega_{2} - \rho_{1}\omega_{1}) \partial_{x}^{-1} \eta \right) - (\omega_{2} - \omega_{1}) \tilde{G}_{12}(\eta) \left(\frac{\eta^{2}}{2} \right), \tag{C 9}$$

and

$$q_2 = \tilde{G}_{21}(\eta) \left(p + \frac{1}{2} (\rho_2 \omega_2 - \rho_1 \omega_1) \partial_x^{-1} \eta \right) + (\omega_2 - \omega_1) \tilde{G}_{22}(\eta) \left(\frac{\eta^2}{2} \right), \tag{C 10}$$

where

$$\begin{split} \tilde{G}_{11}(\eta) &= (\rho_2 G_l^{-1}(\eta) G_u(\eta) - \rho_1)^{-1}, \\ \tilde{G}_{12}(\eta) &= \tilde{G}_{11}(\eta) G_l^{-1}(\eta) \partial_x, \\ \tilde{G}_{21}(\eta) &= G_l^{-1}(\eta) G_u(\eta) \tilde{G}_{11}(\eta), \\ \tilde{G}_{22}(\eta) &= G_l^{-1}(\eta) (1 - G_u(\eta) \tilde{G}_{11}(\eta) G_l^{-1}(\eta)) \partial_x. \end{split}$$

Using the non-local formulation, we can readily find the symbol associated with the linear part of the second variation of the Hamiltonian. We readily find that the leading-order terms of G_u and G_l are given by

$$G_{u0} = -k \tanh(kh_1), \quad G_{k0} = k \tanh(kh_2).$$
 (C 12a,b)

This then readily allows us to find the leading-order symbols of every other operator defined thus far, and therefore we can ultimately find the spectrum associated with the operator

$$\delta^{2}H = \begin{pmatrix} g(\rho_{2} - \rho_{1}) - \frac{\tilde{\omega}^{2}}{4}H_{11} & \frac{\tilde{\omega}}{2}H_{21}^{\dagger} \\ \frac{\tilde{\omega}}{2}H_{21} & H_{22} \end{pmatrix}, \quad (C13)$$

where

$$H_{11} = \partial_{x}^{-1} (\rho_{2} \tilde{G}_{210} G_{l0} \tilde{G}_{210} - \rho_{1} \tilde{G}_{110} G_{u0} \tilde{G}_{110}) \partial_{x}^{-1}, H_{21} = (\rho_{2} \tilde{G}_{210} G_{l0} \tilde{G}_{210} - \rho_{1} \tilde{G}_{110} G_{u0} \tilde{G}_{110}) \partial_{x}^{-1}, H_{22} = \rho_{2} \tilde{G}_{210} G_{l0} \tilde{G}_{210} - \rho_{1} \tilde{G}_{110} G_{u0} \tilde{G}_{110},$$
(C 14)

and

$$\tilde{\omega} = \rho_1 \omega_1 - \rho_2 \omega_2. \tag{C 15}$$

C.1. Linearization about the trivial interface

After non-dimensionalizing, if we linearize around a flat solution travelling with the bifurcating speed $c_0 = \Omega_+(k_0)/k_0$, we find that the corresponding linearized spectrum is given by

$$\lambda_{\pm} = \mathrm{i}(ck + \Omega_{\pm}(k)), \quad \Omega_{\pm}(k) = \frac{1}{2} \left(-\tilde{\omega}\mathcal{T}_k \pm \mathrm{sgn}(k) \sqrt{\mathcal{T}_k^2 \tilde{\omega}^2 + 4(\rho - 1)k\mathcal{T}_k} \right), \tag{C 16a,b}$$

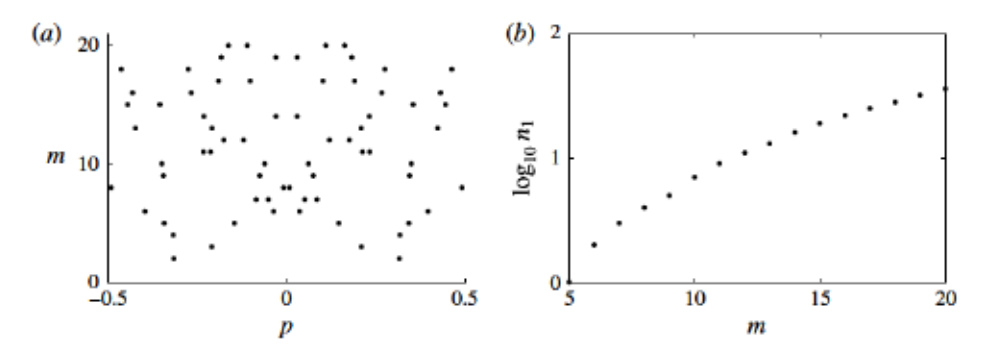


FIGURE 19. (a) Order of resonance, m, as a function of the Floquet parameter p for $\omega_1 = 0$, $\omega_2 = 0$, $\mu = \sqrt{0.1}$, $\delta = 4$ and $\rho = 1.028$. (b) Log plot of the values n_1 as a function of the order of resonance m.

and

$$T_k = \frac{\tanh(\mu k) \tanh(\mu \delta k)}{\mu(\rho \tanh(\mu k) + \tanh(\mu \delta k))},$$
 (C 17)

where we note that $\Omega_{\pm}(-k) = -\Omega_{\pm}(k)$. The corresponding Krein signatures for the two branches of spectra are found to be

$$\kappa(\lambda_{\pm}) = \pm \operatorname{sgn}(k)\operatorname{sgn}\left(c_0 - \frac{\Omega_{\pm}}{k}\right).$$
 (C 18)

Similar formulas appear in Deconinck & Trichtchenko (2016). Following then the approach in resonant interaction theory Dias & Kharif (1999), we likewise see that all potential non-zero amplitude instabilities must emanate from the 'collision' of two elements of the spectrum, say

$$\lambda_{\pm}(n_1+p) = \lambda_{\pm}(n_2+p), \quad n_i \in \mathbb{Z}, \tag{C 19a,b}$$

which is equivalent to the multi-wave mixing formula

$$\Omega_{\pm}(n_1 + p) - \Omega_{\pm}(n_2 + p) = (n_2 - n_1) \frac{\Omega_{+}(k_0)}{k_0},$$

$$= m\Omega_{+}(k_0), \qquad (C 20)$$

where we have set $n_2 - n_1 = mk_0$, or

$$k_2 - k_1 = mk_0, \quad k_j = n_j + p.$$
 (C21a,b)

Here we call m the order of the resonant interaction, and we see that the mth-order resonant interaction corresponds to a m+2 wave mixing problem.

By setting $n_2 = k_1 + mk_0$ and then varying m from 1 to some chosen value, we can use numerical root finding to determine k_1 and thus $n_1 + p$ given that $p \in [-1/2, 1/2)$. Using this then, we can track at which Floquet parameters p we have resonances involving opposite Krein signature eigenvalue collisions. Taking $\omega_1 = \omega_2 = 0$, $\rho = 1.028$, $\delta = 4$ and $\mu = \sqrt{0.1}$, we then get the plot in figure 19 for $1 \le m \le 20$. As we can see, there is no potentially unstable resonance until m = 5, after which several

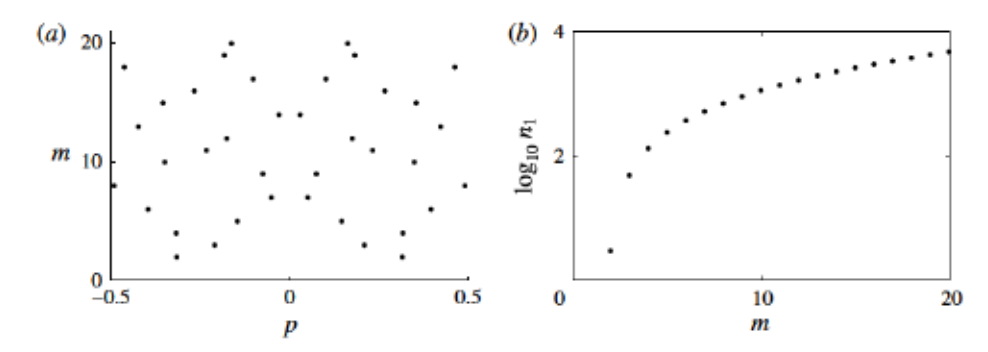


FIGURE 20. (a) Order of resonance, m, as a function of the Floquet parameter p for $\omega_1 = -1$, $\omega_2 = 1$, $\mu = \sqrt{0.1}$, $\delta = 4$ and $\rho = 1.028$. (b) Log plot of the values n_1 as a function of the order of resonance m.

mechanisms for instability are present. We also note that n_1 is of the order of 40 or so when m = 20.

In constrast, when we add vorticity by setting $\omega_1 = -1$ and $\omega_2 = 1$, thereby generating figure 20, while m = 2 and 4 become possible mechanisms for instability generation, the higher-order wave mixing corresponding to larger values of m corresponds to markedly higher wavenumbers than in the zero-vorticity case. Thus, in some sense, the presence of vorticity stabilizes the problem by pushing instabilities out to far higher frequencies.

REFERENCES

ABLOWITZ, M., FOKAS, A. & MUSSLIMANI, Z. 2006 On a new non-local formulation of water waves. J. Fluid Mech. 562, 313–343.

AKERS, B. F., AMBROSE, D., POND, K. & WRIGHT, J. 2016 Overturned internal capillary–gravity waves. Eur. J. Mech. (B/Fluids) 57, 143–151.

APPEL, J. 2004 Oceanic internal wavs and solitons. In Synthetic Aperture Radar Marine User's Manual, pp. 189–206. U.S. Department of Commerce.

ASHTON, A. & FOKAS, A. 2011 A non-local formulation of rotational water waves. J. Fluid Mech. 689, 129-148.

CHOI, W. 2009 Nonlinear surface waves interacting with a linear shear current. Maths Comput. Simul. 80 (1), 29–36.

CONSTANTIN, A. 2011 Nonlinear Water Waves with Applications to Wave-Current Interactions and Tsunamis. SIAM.

CRAIG, W., GUYENNE, P. & KALISCH, K. 2005a Hamiltonian long-wave expansions for free surfaces and interfaces. Commun. Pure Appl. Maths 58, 1587–1641.

CRAIG, W., GUYENNE, P., NICHOLLS, D. P. & SULEM, C. 2005b Hamiltonian long-wave expansions for water waves over a rough bottom. Proc. R. Soc. Lond. A 461, 839–873.

CURTIS, C. & DECONINCK, B. 2010 On the convergence of Hill's method. Maths Comput. 79, 169–187.

CURTIS, C., OLIVERAS, K. & MORRISON, T. 2016 Shallow waves in density stratified shear currents. Eur. J. Mech. (B/Fluids) (accepted).

DALRYMPLE, R. 1974 Water waves on a bilinear shear current. In *Proc. 14th Conf. on Coastal Engng.* (ed. B. Edge), pp. 626-641. American Society of Civil Engineers.

DECONINCK, B. & KUTZ, J. 2006 Computing spectra of linear operators using the Floquet-Fourier-Hill method. J. Comput. Phys. 219, 296–321.

- DECONINCK, B. & OLIVERAS, K. 2011 The instability of periodic surface gravity waves. J. Fluid Mech. 675, 141–167.
- DECONINCK, B. & TRICHTCHENKO, O. 2016 High-frequency instabilities of small-amplitude solutions of Hamiltonian PDEs. DCDS-B (to appear).
- DIAS, F. & KHARIF, C. 1999 Nonlinear gravity and capillary-gravity waves. Annu. Rev. Fluid Mech. 31, 301–346.
- FARMER, D. & ARMI, L. 1999 The generation and trapping of solitary waves over topography. Science 283, 188–191.
- FOKAS, A. S. 2008 A Unified Approach to Boundary Value Problems, vol. 78. SIAM.
- FRANCIUS, M. & KHARIF, C. 2006 Three-dimensional instabilities of periodic gravity waves in shallow water. J. Fluid Mech. 561, 417–437.
- GRUE, J., JENSEN, A., RUSØAS, P.-O. & SVEEN, J. K. 1999 Properties of large-amplitude internal waves. J. Fluid Mech. 380, 257–278.
- HAUT, T. & ABLOWITZ, M. 2009 A reformulation and applications of interfacial fluids with a free surface. J. Fluid Mech. 631, 375–396.
- HELFRICH, K. & MELVILLE, W. 2006 Long nonlinear internal waves. Annu. Rev. Fluid Mech. 38, 395–425.
- HUR, V. & JOHNSON, M. A. 2015 Modulational instability in the whitham equation with surface tension and vorticity. Nonlinear Anal. Theory Meth. Applics. 129, 104–118.
- Ko, J. & Strauss, W. 2008 Effect of vorticity on steady water waves. J. Fluid Mech. 608, 197-215.
- LUKE, J. 1967 A variational principle for a fluid with a free surface. J. Fluid Mech. 27, 395-397.
- McLean, J. W. 1982a Instabilities of finite-amplitude gravity waves on water of finite depth. J. Fluid Mech. 114, 331–341.
- McLean, J. W. 1982b Instabilities of finite-amplitude water waves. J. Fluid Mech. 114, 315-330.
- MOLER, C. & STEWART, G. 1973 An algorithm for generalized matrix eigenvalue problems. SIAM J. Numer. Anal. 10, 241–256.
- OLIVERAS, K., SPRENGER, P. & VASAN, V. 2016 The instability of traveling waves with vorticity: Part I, infinite depth (in preparation).
- OLIVERAS, K. & VASAN, V. 2013 A new equation describing travelling water waves. J. Fluid Mech. 717, 514-522.
- OSBORNE, A. & BURCH, T. 1980 Internal solitons in the Andaman Sea. Science 208, 451-460.
- PULLIN, D. & GRIMSHAW, R. 1983 Interfacial progressive gravity waves in a two-layer shear flow. Phys. Fluids 26, 1731–1739.
- PULLIN, D. & GRIMSHAW, R. 1986 Stability of finite-amplitude interfacial waves. Part 3. The effect of basic current shear for one-dimensional instabilities. J. Fluid Mech. 172, 277–306.
- PULLIN, D. & GRIMSHAW, R. 1988 Finite-amplitude solitary waves at the interface between two homogeneous fluids. *Phys. Fluids* 31, 3550–3559.
- DA SILVA, A. T. & PEREGRINE, D. 1988 Steep, steady surface waves on wter of finite depth with constant vorticity. J. Fluid Mech. 195, 281–302.
- SIMMEN, J. & SAFFMAN, P. 1985 Steady deep-water waves on a linear shear current. Stud. Appl. Maths 75, 35-57.
- SWAN, C., CUMMINS, I. & JAMES, R. 2001 An experimental study of two-dimensional surface water waves propagating on depth-varying currents. Part 1. Regular waves. J. Fluid Mech. 428, 273–304.
- THOMAS, R., KHARIF, C. & MANNA, M. 2012 A nonlinear schrödinger equation for water waves on finite depth with constant vorticity. Phys. Fluids 24 (12), 127102.
- VANDEN-BROECK, J. 1994 Steep solitary waves in water of finite depth with constant vorticity. J. Fluid Mech. 274, 339–348.
- VASAN, V. & OLIVERAS, K. 2014 Pressure beneath a traveling wave with constant vorticity. Discrete Continuous Dyn. Syst. 34, 3219–3239.